Experiments in Fluids (2025) 66:104
https://doi.org/10.1007/s00348-024-03949-z

RESEARCH ARTICLE

Data-driven spatiotemporal analysis of cloud cavitation by means of spectral proper orthogonal decomposition

Grigorios Hatzissawidis[1] · **Moritz Sieber**[2] · **Kilian Oberleithner**[2] · **Peter F. Pelz**[1]

Received: 19 June 2024 / Revised: 31 October 2024 / Accepted: 18 December 2024

Abstract

The global dynamics of cloud cavitation are not always obvious; cloud cavitation may exhibit chaotic, multimodal and intermittent behaviour, where dominant flow structures are hidden to the naked eye. To address this, spectral proper orthogonal decomposition (SPOD) is applied, a method that can continuously transition between proper orthogonal decomposition (POD) and discrete Fourier transformation (DFT)/dynamic mode decomposition (DMD). This provides the opportunity to break down the complex dynamics of interacting and transient processes into interpretable modal bases. Experiments were conducted in a high-speed cavitation tunnel using a two-dimensional NACA 0015 hydrofoil at a fixed Reynolds number of 8×10^5 and an incidence of 12° for varying cavitation numbers. The cavitation was recorded using a synchronised dual-camera set-up with simultaneously captured pressure signals. Shockwave-driven and re-entrant flow-driven cloud shedding is identified, as well as the transition regime in between, exhibiting more complex behaviour. The transition from shockwave-driven to re-entrant flow-driven cloud cavitation is smooth, with shockwaves becoming more dominant as the cavitation number decreases. SPOD modes allow for a frequency and amplitude variation, which successfully decomposes the data into the dominant modes, whereas classical modal decomposition methods such as POD and DMD do not provide interpretable decompositions. SPOD grants access to a transient analysis of the data via the SPOD time coefficients. We validate the SPOD results using space–time plots and power spectral density (PSD) of the pressure signals, being in good agreement with the SPOD spatial modes and time coefficients. The complex time coefficients give access to instantaneous mode frequencies and allow calculating a standard deviation of the frequency modulation of the modes. The findings provide a deep insight into the spatial and temporal behaviour of cloud cavitation and support the understanding of its physics.

1 Introduction

Cloud cavitation, a technically significant manifestation of cavitation, has engaged engineers for over fifty years. It is associated with a strong periodicity, where large-scale cavitation clouds detach and collapse. Cloud cavitation occurs in ship propellers or other hydraulic devices such as pumps, turbines, nozzles, as well as mechanical heart valves. This results in vibration, noise, efficiency loss and mechanical material damage, i.e. cavitation erosion, resulting in failure of components up to whole fluid systems. Cloud detachment and subsequent collapse is the main source of cavitation erosion, cf. Petkovšek and Dular (2013); Dular and Petkovšek (2015); Hatzissawidis et al. (2021, 2022).

Cavitation is generally associated with various interacting physical phenomena such as hydrodynamic instabilities, compressible effects, i.e. shockwaves, transport phenomena such as diffusion and convection, turbulence

✉ Grigorios Hatzissawidis
grigorios.hatzissawidis@tu-darmstadt.de

Moritz Sieber
moritz.sieber@tu-berlin.de

Kilian Oberleithner
oberleithner@tu-berlin.de

Peter F. Pelz
peter.pelz@tu-darmstadt.de

[1] Chair of Fluid Systems, Technische Universität Darmstadt, Otto-Berndt-Str. 2, Darmstadt 64287, Germany

[2] Laboratory for Flow Instabilities and Dynamics, Institut für Strömungsmechanik und Technische Akustik, Technische Universität Berlin, Müller-Breslau-Straße 8, Berlin 10623, Germany

and boundary layer effects leading to complex intermittent as well as multimodal behaviour.

In the case of cloud cavitation, two distinct formation mechanisms are relevant from lower to higher cavitation numbers: (I) shockwave-driven cloud formation and (II) re-entrant flow-driven cloud formation, both causing large-scale cavitation clouds. A further increase in the cavitation number leads to (III) sheet cavitation where interfacial instabilities result in small-scale cloud formation and irregular shedding. In this study, we are focusing on the global dynamics of large-scale cloud cavitation due to (I) shockwave propagation and (II) re-entrant flow.

Knapp (1955, 1956) was the first to describe the periodic behaviour of cloud cavitation qualitatively in his pioneer studies. He discovered the existence of a (II) re-entrant flow that originates in the cavity closure region and causes the sheet cavity to break off when it reaches the cavity leading edge. However, the re-entrant flow can break the sheet prematurely, leading to an earlier break-off.

Years later, Wade and Acosta (1966) reported the strong oscillation of large-scale cloud cavitation under special conditions. Furness and Hutton (1975) confirmed these observations experimentally and developed an unsteady two-dimensional model using irrotational flow theory to describe the periodic behaviour.

More recently, the cloud formation mechanism due to a re-entrant flow was studied experimentally and theoretically on a convergent–divergent nozzle by Pelz et al. (2017), who derived an analytical model to predict the transition from sheet to cloud cavitation depending on a critical Reynolds number Re_c. The re-entrant flow originates in the cavity closure region due to the stagnation point flow and flows upstream beneath the cavity sheet. Depending on the momentum and dissipation, it can either reach the cavity leading edge or result in premature break-off of the cavity sheet, Pelz et al. (2017).

Other researchers reported that a high adverse pressure gradient at the cavity closure region is necessary for the re-entrant flow to develop, cf. Gopalan and Katz (2000); Laberteaux and Ceccio (2001); Callenaere et al. (2001).

For many years, re-entrant flow was recognised as the sole mechanism of cloud shedding, dictating the global cavitation dynamics. However, condensation shockwaves that influence the cavitation dynamics were already hypothesised by Jakobsen (1964) due to the rapid decrease of the speed of sound in a gas/liquid mixture compared to a single-phase flow, cf. Brennen (2013). Stutz and Reboud (1997) observed that the cloud collapse influences the cavity growth. This was later confirmed by Leroux et al. (2005) and Coutier-Delgosha et al. (2007). Kawanami et al. (1997) also reported shockwaves, although the authors claimed that the re-entrant flow was responsible for cloud shedding.

Reisman et al. (1998) paved the way for a research field on the dominant role of shockwaves in cloud cavitation besides the re-entrant flow. The transition from re-entrant flow-driven to shockwave-driven cavitation is associated with an abrupt change in cavitation dynamics, as reported by Arndt et al. (2000) and Kjeldsen et al. (2000). The abrupt transition from re-entrant flow-driven cloud cavitation to shockwave-driven cloud cavitation occurs when the cavity sheet length equals the chord length of the hydrofoil, cf. Hatzissawidis et al. (2025).

Wu et al. (2019) addressed this phenomenon as well in an experimental study about a NACA0015 hydrofoil, where multimodal behaviour occurred, i.e. both shockwaves and re-entrant flow lead to complex and interacting dynamics.

A detailed investigation of shockwave-driven cloud cavitation was conducted experimentally by Ganesh et al. (2016) using X-ray densitometry and high-speed visualisation techniques, and numerically by Budich et al. (2018) on the same convergent–divergent sharp wedge. There, shockwave-driven shedding was reported when the cavitation number is decreased below a certain value, while above this value intermittent re-entrant flow-driven shedding can be observed.

Recent experimental studies conducted by Bhatt et al. (2023) further reveal that there is a specific probability for re-entrant flow or shockwave-driven cloud shedding depending on the cavitation number and Mach number described by a likelihood function, rather than clearly isolated regimes, where either regime (I) or regime (II) occurs.

Since the global cavitation dynamics can exhibit multimodal, intermittent and chaotic behaviour with interacting complex phenomena depending on various conditions such as the operation point, geometry and nuclei content as shown by recent studies of Venning et al. (2022), it may demand great effort to capture the dominant, coherent flow patterns from the cavitating flow field.

Classical decomposition methods, as well as other existing techniques, often fail or require extensive prior knowledge to decompose the flow field in a physically meaningful way. A detailed discussion is given in Sect. 2.

In the present work, we apply a modal decomposition technique called spectral proper orthogonal decomposition (SPOD) developed by Sieber et al. (2016) to the high-speed recordings to identify the temporal frequencies and the corresponding spatial modes from the cavitating flow field. In addition to a dual-camera high-speed imaging set-up that captures the cavitation from the top and the side view, pressure data were recorded simultaneously using two piezoelectric pressure transducers and a hydrophone, allowing additional insight into the shedding mechanisms.

The paper is organised as follows: A brief theoretical overview of the SPOD technique and its benefits is provided in Sect. 2, introducing the main idea of this technique as well as existing studies regarding cavitation and modal decomposition. Next, we provide a detailed overview of the experimental set-up considering measurement techniques, transducers, high-speed cameras, uncertainties and metadata (Sect. 3). An overview of the cavitation regimes and the associated cavitation dynamics, depending on the cavitation number σ, is given in Sect. 4. Besides the aforementioned (I) shockwave-driven cloud cavitation regime and (II) re-entrant flow-driven cloud cavitation regime, we consider a transition regime, TR (I)–(II), where both mechanisms play a role. Detailed analyses are carried out for selected operation points in Sects. 4.1 to 4.3. We compare the power spectral density (PSD) of the pressure transducer signal and the SPOD results, and conduct a transient analysis of the spatial cavitating structures of the modes identified by the SPOD. Finally, we present our conclusions in Sect. 5.

2 Spectral proper orthogonal decomposition (SPOD)

The introduction of the proper orthogonal decomposition (POD), also known as Karhunen–Loéve transform, principal component analysis (PCA) and singular value decomposition, into the research field of fluid mechanics, especially regarding turbulent flows, dates back to Lumley (1970) and Sirovich (1987). The latter developed the so-called *method of snapshots*, reducing the computational demand.

Besides POD, dynamic mode decomposition (DMD) developed by Schmid (2010) is also a widely used modal decomposition technique where modes are constructed from the decomposition of an operator that linearly approximates the temporal propagation observed in the data. The discrete Fourier transformation (DFT) is related to DMD, although it differs in providing growth and decay rates of the modes (Tu et al. 2014). Taira et al. (2017) give a detailed survey of the most common techniques and applications considering modal decomposition in fluid mechanics.

POD ranks the modes according to the energy content or variance K and provides orthogonality in space. In contrast, DMD assigns a distinct frequency to each mode, which is not valid for most flow patterns in turbulent flows. Moreover, DMD has no default ranking, and high effort may be necessary to identify the most dominant modes. Another property of DMD and DFT is that fluctuations in frequency lead to a spectral leakage to neighbouring modes close to the most dominant frequency. On the contrary, POD provides multifrequency modes and tends to contain modes at different timescales, impeding physical interpretation, cf. Sieber et al. (2016).

To address these drawbacks, SPOD was introduced by Sieber et al. (2016). On the basis of POD, it bridges the gap between DFT or DMD and POD by applying a filter to the correlation matrix; this is put into practice by a single parameter called filter size. This filter size allows for a continuous shift between POD and DFT. A further comparison between POD, SPOD and DFT is also discussed in Appendix C.

In recent years, modal decomposition techniques found their way into cavitation research to capture the global dynamics of cavitating flows. Prothin et al. (2016) applied DMD and POD to high-speed recordings across various cavitation regimes on a NACA 0015 hydrofoil, conducting a comparative analysis of both methods. Smith et al. (2020b, 2020a) applied a related spectral POD variant proposed by Towne et al. (2018) to high-speed recordings of a cavitating flow about a three-dimensional stiff and flexible hydrofoil to identify the dominant modes of the cavitating flow field. Barwey et al. (2020) applied cluster-based reduced-order modelling (CROM), which requires the specification of the number of clusters, to density fields from time-resolved X-ray measurements of cloud cavitation, capturing its multimodal behaviour.

In this study, we demonstrate that SPOD is capable of capturing the global dynamics of a cavitating flow about a two-dimensional NACA 0015 hydrofoil without having much prior knowledge of the flow. SPOD enables transient analysis through the use of time coefficients, eliminating the need to specify a fixed amount of data beforehand for convergence. The specific implementation of SPOD for this task is presented below.

Typically, the input data for modal decomposition techniques are velocity fields obtained from particle image velocimetry (PIV) as well as from numerical simulations. In the present work, we apply SPOD to greyscale values of high-speed recordings from a dual-camera set-up using the side and the top views of the cavitating flow field. Greyscale values can be linked to the local gas/vapour content, although they do not represent an actual physical quantity, limiting its physical interpretation. When decomposing velocity data, these can be interpreted as kinetic energy, whereas here we interpret them as variances of the recorded intensity fluctuations.

In this context, a brief mathematical description of SPOD is given. For a detailed explanation, we refer to Sieber et al. (2016). We separate the greyscale intensity field $\mathbf{I}(\mathbf{x}, t)$, which depends on time t and spatial coordinate $\mathbf{x}$, into the mean $\bar{\mathbf{I}}(\mathbf{x})$ and the fluctuating part $\mathbf{I}'(\mathbf{x}, t)$,

$$\mathbf{I}(\mathbf{x}, t) = \bar{\mathbf{I}}(\mathbf{x}) + \mathbf{I}'(\mathbf{x}, t), \tag{1}$$

and decompose solely the fluctuating part into the time coefficients $a_i(t)$ and the spatial modes $\Phi_i(\mathbf{x})$, similar to the separation of variables method, obtaining

$$\mathbf{I}(\mathbf{x}, t) = \bar{\mathbf{I}}(\mathbf{x}) + \sum_{i=1}^{N} a_i(t)\, \Phi_i(\mathbf{x}), \tag{2}$$

where N denotes the number of frames, also called snapshots, and thus the number of modes. The decomposition is based on the temporal correlation matrix $\mathbf{R} \in \mathbb{R}^{N \times N}$ with its elements R_{ij} calculated from the inner product of the fluctuating parts of the snapshots $\mathbf{I}'\left(\mathbf{x}, t_i\right) \in \mathbb{R}^M$, with M being the number of the spatially distributed recorded points:

$$R_{ij} = \mathbf{I}'\left(\mathbf{x}, t_i\right) \cdot \mathbf{I}'\left(\mathbf{x}, t_j\right). \tag{3}$$

Usually, $N \ll M$ is valid in flow visualisation techniques. The eigenvectors and eigenvalues of the correlation matrix are the temporal coefficients $\mathbf{a}_i$ and the corresponding mode variances λ_i with $i = 1, \dots, N$, respectively:

$$\mathbf{R}\, \mathbf{a}_i = \lambda_i\, \mathbf{a}_i. \tag{4}$$

The method described above is the classical POD and can be easily computed by a singular value decomposition of the data matrix $\left[\mathbf{I}'\left(\mathbf{x}, t_1\right), \dots, \mathbf{I}'\left(\mathbf{x}, t_N\right)\right]$, cf. Holmes et al. (2012).

The basic idea of SPOD is to apply a filter on the correlation matrix $\mathbf{R}$. A Gaussian filter is used, which provides a smooth response in the time and frequency domain. The standard deviation is chosen to be equal to the cut-off frequency of a box filter with half the size, cf. Sieber et al. (2016). With the filter coefficients vector $\mathbf{g} \in \mathbb{R}^{2N_\mathrm{f}+1}$ and filter width N_f, the components of the filtered correlation matrix $\mathbf{S}$ are given by

$$S_{ij} = \sum_{k=-N_\mathrm{f}}^{N_\mathrm{f}} g_k\, R_{i+k,j+k}. \tag{5}$$

In the present work, we use periodic boundary conditions for the correlation matrix $\mathbf{R}$.

As in the case of the classical POD, the SPOD temporal coefficients $\mathbf{b}_i$ and mode variances μ_i are eigenvectors and eigenvalues of the filtered correlation matrix:

$$\mathbf{S}\, \mathbf{b}_i = \mu_i\, \mathbf{b}_i. \tag{6}$$

The temporal coefficients are scaled with the mode variances and preserve their orthogonality,

$$\frac{1}{N}\, \mathbf{b}_i \cdot \mathbf{b}_j = \mu_i\, \delta_{ij}, \tag{7}$$

where δ_{ij} denotes the Kronecker delta. The corresponding ith spatial mode is computed by projecting the snapshots onto the temporal coefficients:

$$\Psi_i(\mathbf{x}) = \frac{1}{N\, \mu_i} \sum_{j=1}^{N} b_i\left(t_j\right) \mathbf{I}'\left(\mathbf{x}, t_j\right). \tag{8}$$

It should be mentioned that the spatial modes $\Psi_i(\mathbf{x})$ are no longer orthogonal. However, the total amount of correlation that equals the turbulent kinetic energy for velocity data is maintained:

$$\sum_{i=1}^{N} \mu_i = \sum_{i=1}^{N} \lambda_i. \tag{9}$$

Hence, the traces of the correlation matrix and the filtered correlation matrix are equal. The original data can be recomposed exactly by

$$\mathbf{I}(\mathbf{x}, t) = \bar{\mathbf{I}}(\mathbf{x}) + \sum_{i=1}^{N} b_i(t)\, \Psi_i(\mathbf{x}). \tag{10}$$

As mentioned above, SPOD allows switching between POD, $N_\mathrm{f} = 0$, and DFT, $N_\mathrm{f} \rightarrow \infty$, for the case of a Gaussian filter applied to the correlation matrix. However, the result remains almost the same for a filter width larger than the snapshot number, $N_\mathrm{f} > N$; thus, the DFT is computed for $N_\mathrm{f} = N$ using a box filter instead of a Gaussian filter, cf. Sieber et al. (2016).

In between these two special cases, N_f has to be appropriately set depending on the underlying problem. Promising results are obtained if the filter width matches a characteristic timescale of the flow, i.e. the filter width is equal to one or two periods of the dominant mode, cf. Sieber et al. (2021). In the present work, we identify a characteristic frequency from the pressure signal of the piezoelectric transducer to set an appropriate filter width.

After the SPOD modes have been calculated, the mode pairs should be assigned for the investigation of periodic phenomena, similar to the real and imaginary parts in DFT. For this purpose, the modes are paired according to the spectral proximity among all modes. This is implemented according to Sieber et al. (2016) using a DMD of the temporal coefficients $\mathbf{b}_i$ to calculate the harmonic correlation (cross-spectral density with a $\pi/2$ phase shift). A DMD is used rather than a DFT because a rank reduction in the DMD allows rejecting measurement noise, cf. Tu et al. (2014).

We consider N_c SPOD modes containing 95 % of the total variance to eliminate noise. In the following, we define the variance K_i of mode i using the remaining N_c modes as

$$K_i := \frac{\mu_i}{\sum_{j=1}^{N_\mathrm{c}} \mu_j}. \tag{11}$$

In this study, we feed both views, namely the side view and the top view, using $N = 8001$ frames per view into the SPOD algorithm. To reasonably integrate both views into the SPOD algorithm, we initially normalise the greyscale values to a range from 0 to 1. In addition, we apply a uniform weighting across the frame to compensate for the difference in pixel counts.

The dual-camera set-up, cf. Sect. 3, introduces non-uniformities in the cavitation illumination, as it required a balance between achieving homogeneous lighting and maintaining visibility for both the side and top views. The illumination is more intense on the side where the LED light source passes through the acrylic glass to illuminate the cavitation for the side view. To address these non-uniformities, we implemented a weight matrix in the SPOD algorithm specifically for the top view. However, no significant differences were observed between the results with and without the weight matrix in terms of SPOD mode detection. The harmonic correlation and variance remained unaffected, and the same physical phenomena were detected in both cases. Consequently, we opted to proceed without using the weight matrix, relying instead on the raw high-speed recordings.

Nonetheless, we applied masks to the top view to cover the side walls and, in the side view, to cover the hydrofoil cross section and the piezoelectric transducer, to eliminate reflections from these components. The filter width is chosen to be two to three times the period T in frames of the fundamental mode, $2 < N_\mathrm{f}/T < 3$.

The present work uses the SPyOD package, which can be accessed via the GitHub repository (Hatzissawidis and Sieber 2023).

3 Experimental set-up and techniques

Experiments were carried out at the high-speed water cavitation tunnel at the Technische Universität Darmstadt (Fig. 1), which is a closed circuit system where the pressure may be varied from near vacuum to 16 bar, cf. Hatzissawidis et al. (2025). Since the test rig is designed to investigate mass loss due to cavitation erosion on hydrofoils, high flow velocities up to $U = 30\,\mathrm{m/s}$ can be reached in the test section.

The test section has a rectangular cross-sectional area with a height of 70 mm, a depth of 25 mm and a length of 462 mm. Three of the test section walls are made from acrylic glass ensuring optical accessibility, cf. Fig. 2. Wetted components like piping and the pressure vessel, capacity of $0.89\,\mathrm{m}^3$, are made from stainless steel to avoid corrosion.

Flow circulation is generated using a KSB Etanorm ETN 125-100-400 single-stage volute casing pump with a 6-bladed impeller. The fluid flows into the vessel through a submerged pipe so that nuclei generation is avoided due to the impact on the free surface, cf. Fig. 1.

The pipe diameter of 100 mm behind the pump expands to 133 mm over a diffuser with a length of 169 mm. This circular cross-sectional area turns into the rectangular cross-sectional area in the test section over a nozzle of length 105 mm whose contour is a fifth-degree polynomial. A diffuser of the same shape leads the outflow behind the test section into a circular cross-sectional area with a diameter of 133 mm.

The flow into the test section at a position 93 mm upstream of the hydrofoil's rotational axis was characterised for an empty test section and a non-cavitating flow using a one-dimensional laser Doppler velocimetry (LDV) system of the manufacturer Dantec Dynamics with a Coherent Genesis MX 514 STM continuous-wave solid-state laser. An extensive analysis of the inflow characteristics can be found

Fig. 1 Schematic overview of the high-speed water cavitation tunnel at Technische Universität Darmstadt

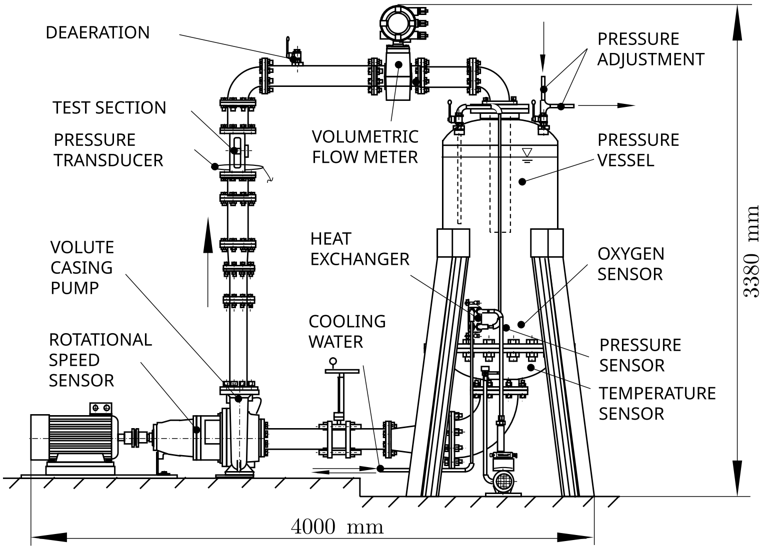

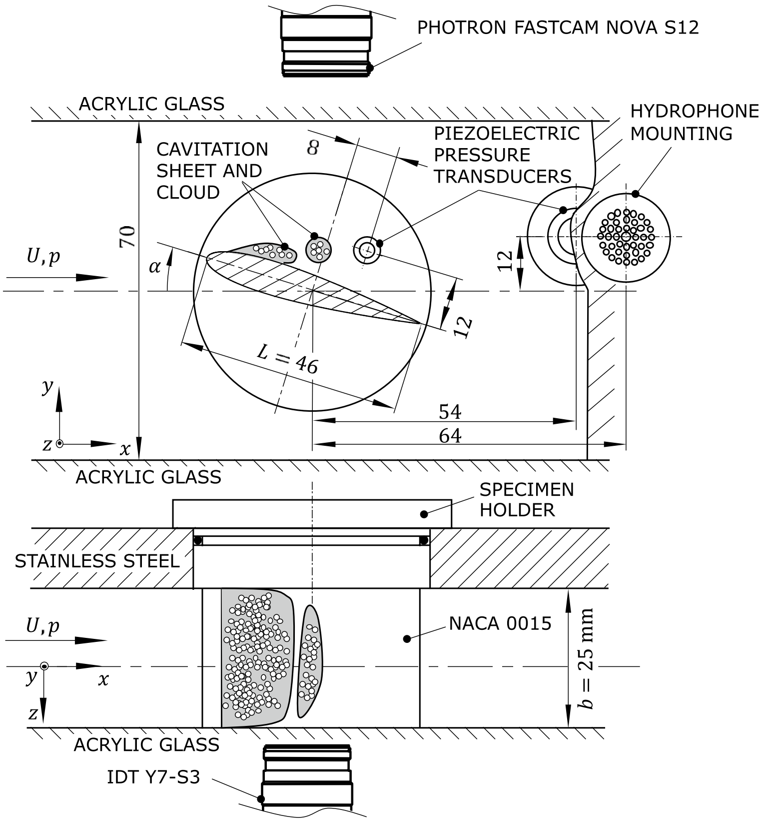

Fig. 2 Side and top view of the test section with the NACA 0015 hydrofoil, the wall-mounted piezoelectric pressure transducers and the hydrophone in the cloud collapse and shedding area

in Appendix D. The flow entering the test section shows no significant non-uniformities, with the relative maximum absolute velocity difference being less than 3%. This value represents the maximum deviation of the velocity at a fixed spatial point from the mean velocity over the entire area outside the boundary layer. The relative mean absolute difference is approximately 1% across all operation points.

The turbulence intensity in the x-direction for the Reynolds numbers under investigation ranges between 3 and 4% in the central region of the test section. Additionally, both the time-resolved upstream pressure, p, and the free-stream velocity, U, exhibit no significant temporal variation, with a coefficient of variation of around 1% across the operating points studied.

A cooling system connected to an external cooling circuit controls the fluid temperature within the vessel in the range of $T = 23.5\,°\mathrm{C} \pm 0.05\,°\mathrm{C}$ using a PT100 temperature sensor, cf. Fig. 1. The dissolved oxygen content of the fluid is set using a VisiFerm DO Arc 120 H0 oxygen sensor mounted in the vessel. The oxygen content within the vessel is kept between 4 and 8 ppm for all measurements in the present study.

The free-stream velocity U in the test section is calculated from the volumetric flow rate captured by an ABB ProcessMaster500 FEP511-125D magnetic flow meter-mounted downstream of the test section, cf. Fig. 1, and has an uncertainty of 0.3 % of reading.

The static pressure is measured at the position 143 mm upstream of the hydrofoil's rotational axis using a Keller PAA-33X absolute pressure transducer that ranges from 0 to 10 bar with an uncertainty of 0.1 % of full scale. The data were received using a National Instruments PCIe-6363 card at a sampling rate of 3000 Hz for 20 s. Measurement uncertainties were estimated according to ISO-GUM (ISO/TMBG Technical Management Board 2010) using the METAS UncLib library.

The experiments were carried out on a two-dimensional NACA0015 hydrofoil made of stainless steel with a nominal chord length of $L = 46$ mm and a span of $b = 25$ mm (Fig. 2). For manufacturing reasons, the NACA 0015 hydrofoil is truncated at the trailing edge resulting in a real chord length of 44 mm. However, the characteristic length remains 46 mm.

The surface of the hydrofoil was polished to achieve a hydraulically smooth finish. Surface roughness measurements were taken using a Mahr Marsurf M310 device, revealing an arithmetic average roughness of $R_a = 0.2\mu$m and a maximum profile height of $R_z = 2.4\mu$m.

The blockage ratio for the NACA0015 hydrofoil at an incidence angle of $\alpha = 12°$ is 16.04% in the set-up used in this study. According to the method outlined by Franc and Michel (2005), the corresponding critical cavitation number due to blockage is calculated as $\sigma_{\mathrm{B}} = 0.42$. This value is notably lower than the cavitation numbers examined in this study. According to the ITTC guidelines, a blockage ratio below 20% is generally recommended to study cavitation patterns (ITTC 2016). This recommendation is further supported by recent numerical and experimental studies conducted by Katsuno and Dantas (2022), which demonstrate that cavitation patterns remain unaffected for blockage ratios below 20%.

The cavitation number and Reynolds number are defined as $\sigma := 2\,(p - p_{\mathrm{v}})/(\varrho\, U^2)$ and $Re := U\,L/\nu$, respectively, where p_{v} is the vapour pressure of water, ϱ is the water density and ν is the kinematic viscosity of the water at temperature T. The cavitation number is adjusted by pressurising the vessel.

High-frequency pressure measurements were taken to capture the transient behaviour of the cavitation and radiated pressure waves due to cloud collapses. Two piezoelectric transducers are flush-mounted on the side wall. The first transducer is a Kistler Type 601CAB, eigenfrequency > 215 kHz, diameter 5.55 mm, with a Kistler 5018A single-channel charge amplifier. It is located in the cloud collapse zone, cf. Fig. 2, and the signal is denoted by $\tilde{p}_1$.

Further downstream, a highly sensitive piezoelectric pressure transducer, Kistler type 701A with a Kistler 5018A single-channel charge amplifier, is mounted in the wake and has an eigenfrequency of 70 kHz and a diameter of 9.5 mm. The signal is denoted by $\tilde{p}_2$. Specimen holder and mounting adapter are made of polyether ether ketone (PEEK) to avoid ground loops.

A Brüel & Kjær (B&K) hydrophone type 8103 with a B&K conditioning amplifier type 2650 is mounted on the opposite side wall of the piezoelectric transducers in a chamber with a flush-mounted hole pattern, see Fig. 2. The signal is denoted by $\tilde{p}_{\mathrm{hy}}$.

These high-frequency data were recorded simultaneously using a National Instruments cDAQ-9189 chassis with a 16-bit National Instruments 9223 voltage input module at a sampling rate of 200 kHz for a sampling time of 20 s to obtain clear spectra.

Simultaneous high-speed recordings were carried out using a synchronised dual-camera set-up which provides the trigger for the high-frequency measurements. The top view of cavitation was recorded by a Photron Fastcam Nova S12 as the sender device with a 12-bit monochrome CMOS sensor and a Carl Zeiss Makro-Planar T* 2/50 mm ZF lens, operated at a frame rate of 18 000 FPS with a resolution of 1024 × 768 px, an exposure time of 6.7 µs and a spatial resolution of 0.078 mm/px. In total, 8001 frames were stored, resulting in a recording time of 0.4445 s.

Cavitation from the side view was synchronously recorded using an IDT MotionPro Y7 S3 monochrome high-speed camera as the receiver device with a 10-bit CMOS sensor and a Carl Zeiss Distagon 1.4/35 mm lens operated at the same synchronised frame rate of 18 000 FPS with a resolution of 1920 × 600 px, an exposure time of 6.7 µs and a spatial resolution of 0.035 mm/px. Illumination was provided by two triggered Veritas Constellation 120 LED lights and one IDT 19-LED.

4 Cavitation regimes and shedding mechanisms

The global shedding dynamics of cavitation depend on numerous parameters such as the Reynolds number, cavitation number, incidence, hydrofoil shape and surface roughness. In this study, the Reynolds number $Re = 8 \times 10^5$ and the incidence $\alpha = 12°$ were kept constant, and the cavitation number was varied from supercavitation, $\sigma = 0.7$, to no cavitation, e.g. single-phase flow, $\sigma = 5.5$. The range covers the entire spectrum between these two extremes. In the spectrum, we define the following regimes as introduced in Sect. 1: (I) shockwave-driven cloud cavitation, (II) re-entrant flow-driven cloud cavitation and (III) sheet cavitation, cf. Fig. 3. We also define the transition regimes in between (I) and (II) and (II) and (III). The high incidence of 12° was selected after conducting an extensive study on the regimes observed at varying incidence. The objective was to identify a clear regime where both re-entrant flow-driven and shockwave-driven cloud cavitation are prominent.

The subdivision into specific regimes is determined based on the SPOD results for each operation point, cf. Fig. 23. When the SPOD identifies multimodal behaviour—specifically the presence of both shockwave-driven cloud cavitation in the low-frequency band and re-entrant flow-driven cloud cavitation in the high-frequency band—the regime is defined as TR (I)–(II). For higher cavitation numbers, cloud cavitation is re-entrant flow-driven (II), while for lower cavitation numbers, it is shockwave-driven (I). The transition from regime (II) to (III) is defined using the same procedure. At higher cavitation numbers, re-entrant flow-driven cloud cavitation vanishes, and a quasi-steady sheet cavitation appears, where small-scale clouds are shed. In the transition regime TR (II)–(III), the shedding intermittently switches between re-entrant flow-driven cloud cavitation and sheet cavitation. The transitions from sheet cavitation (III) to re-entrant flow-driven cloud cavitation (II) and from re-entrant flow-driven cloud cavitation (II) to shockwave-driven cloud cavitation (I) are theoretically and experimentally investigated in Pelz et al. (2017) for a convergent-divergent nozzle and in Hatzissawidis et al. (2025) for the present set-up, respectively.

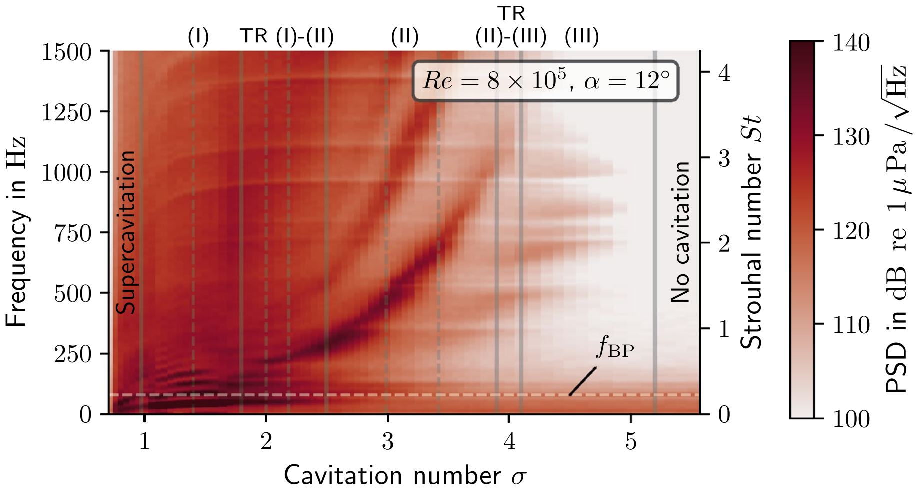

Fig. 3 Welch spectrogram of the pressure signal $\tilde{p}_2$ in dB at constant Reynolds number $Re = 8 \times 10^5$ and incidence $\alpha = 12°$ for varying cavitation number σ. There are three dominant regimes, where the boundaries are denoted by the solid lines (——): (I) shock-wave-driven cloud cavitation, (II) re-entrant flow-driven cloud cavitation and (III) sheet cavitation and transition regimes. The operation points considered in the following analysis are denoted by the dashed lines (- - -).

A first overview of the dynamics observed in the operational range is provided with the Welch spectrogram in Fig. 3. It is obtained using the Welch method similar to Smith et al. (2020b) to calculate the power spectral density (PSD) $\hat{p}/\Delta f$ in $\mathrm{Pa}^2/\mathrm{Hz}$, where $\hat{p}$ is the coefficient of the Fourier transform and Δf is the frequency spacing. We chose a Hanning window with a window size of 20 000 or 0.1 s and an overlap of 50 %.

The presented level of the PSD, also known as the sound pressure level L_{p} in dB, is calculated using the common reference pressure of $p_{\mathrm{ref}} = 1\,\mu\mathrm{Pa}/\sqrt{\mathrm{Hz}}$ as

$$L_{\mathrm{p}} = 10\,\log_{10}\left(\frac{B\,\hat{p}^2/\Delta f}{p_{\mathrm{ref}}^2}\right), \tag{12}$$

according to Bies and Hansen (2009), where $B = 1.5$ is the noise bandwidth for a Hanning window.

The Strouhal number based on the chord length, $St := fL/U$, is given along with the frequency in Hz in the resulting Welch spectrogram in Fig. 3. The horizontal dashed line represents the blade-pass frequency f_{BP}. It can be seen that it does not align with any frequencies related to the cavitation dynamics. Additionally, a study was conducted using various filter sizes to examine how the dominant frequencies change. In all cases, including when no filter was applied, the blade-pass frequency did not appear as a mode in the SPOD results, confirming that the pump operation does not influence the cavitation dynamics.

The Welch spectrogram exhibits two dominant frequency bands: the low-frequency band which is independent of the cavitation number in the range $1 < \sigma < 2.5$ and the high-frequency band within the range $1.8 < \sigma < 4$, which depends on σ. This discontinuous change in the shedding dynamics, cf. Fig. 3, was also observed by Kjeldsen et al. (2000), Smith et al. (2020b) and recently by Bhatt et al. (2023). The emerging dynamics suggest the division of the operational range into the aforementioned regimes, as detailed in the caption of Fig. 3.

It is well known in the case of cavitation driven by re-entrant flow, regime (II), that the fundamental Strouhal number depends on the cavitation number σ. This is reflected by the increasing PSD peak in the Welch spectrogram (Fig. 3). The cavity sheet length increases with decreasing cavitation number, and the re-entrant flow has to travel a longer distance, cf. Pelz et al. 2017.

Based on the aforementioned studies (Kjeldsen et al. 2000; Arndt et al. (2000); Smith et al. 2020b), which associate the low-frequency band—almost independent of the cavitation number—with condensation shockwaves and the high-frequency band-dependent on the cavitation number

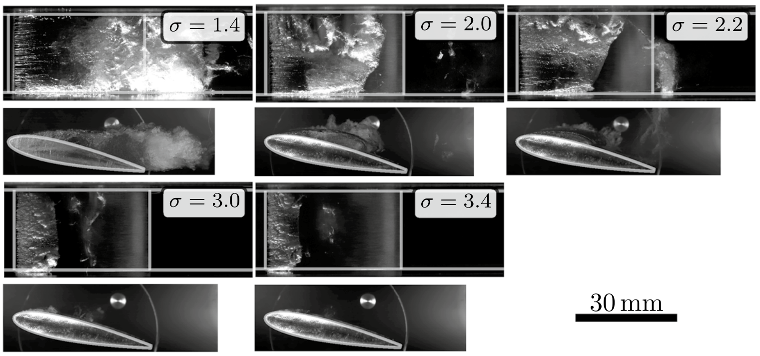

Fig. 4 Top and side view of the cavitation appearance at its maximum sheet length as the cavitation number is increased, Reynolds number $Re = 8 \times 10^5$ and incidence $\alpha = 12°$

with re-entrant flow as the dominant cloud shedding mechanism, we can distinguish between these two mechanisms.

It is noteworthy that in regime (II) the occurrence of upstream propagating shockwaves resulting from a cloud collapse in the preceding cycle may occur, with a higher probability at lower cavitation numbers. This has been recently reported by Bhatt et al. (2023) through the use of X-ray densitometry, a technique that facilitates the differentiation between shockwaves and re-entrant flow.

Additional information on how the frequency of the most dominant mode, also referred to as the fundamental mode, varies with the cavitation number is also provided in Appendix A, for cavitation numbers between $\sigma = 1.4$ and 4.

In the following analysis, we focus on regime (I), TR (I)–(II) and (II) and aim to identify the dominant modes, consisting of a temporal and a spatial part, by applying SPOD to the high-speed recordings. The corresponding

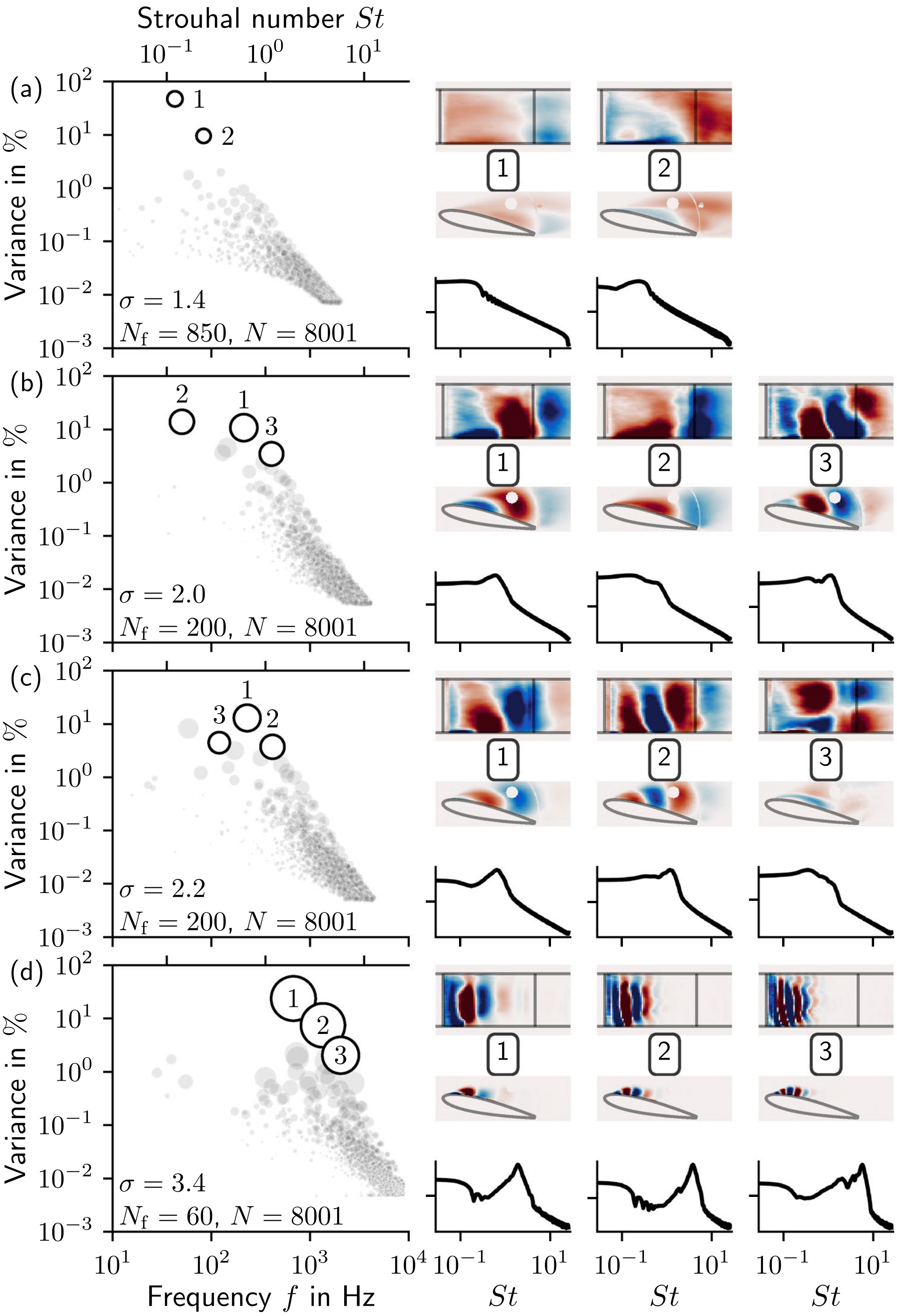

Fig. 5 Left: SPOD spectrum, upper right: real part of the spatial modes, lower right: Welch PSD of the real part of the temporal coefficients for **a** regime (I): $\sigma = 1.4$, **b** TR (I)-(II): $\sigma = 2.0$, **c** TR (I)–(II): $\sigma = 2.2$, **d** regime (II): $\sigma = 3.4$ at $Re = 8 \times 10^5$ and $\alpha = 12°$. A single dot in the SPOD spectrum corresponds to one mode pair, and the size is the harmonic correlation between them

Table 1 Operation points considered in the analysis with important quantities and parameters. The regimes labelled by an asterisk (*) are analysed in more detail in Sects. 4.1 to 4.3

Regime	σ	$\sigma/2\,\alpha$	$\hat{a} := \hat{a}/L$	St_1	K_1 in %	N_f/T_1	Shedding mechanism
(I)*	1.4	3.4	1.43	0.12	47	2.02	Shockwave-driven, presence of re-entrant flow
TR (I) - (II)	2.0	4.8	0.68	0.60	11	2.37	Transition regime, shockwaves and re-entrant flow
TR (I) - (II)*	2.2	5.2	0.60	0.66	13	2.56	Same as above with more dominant re-entrant flow
(II)	3.0	7.1	0.33	1.34	23	2.61	Mainly re-entrant flow
(II)*	3.4	8.2	0.24	1.92	24	2.26	Mainly re-entrant flow

operation points considered here are highlighted by the vertical dashed lines in the Welch spectrogram (Fig. 3).

The side and top view of the appearance of the cavitation at its maximum sheet length $\hat{a}_+$ as the cavitation number increases is shown in Fig. 4. As expected, the cavity sheet length decreases as the cavitation number increases, cf. Table 1.

For the shockwave-driven cavitation regime (I), $\sigma = 1.4$, the sheet extends beyond the hydrofoil (Fig. 4). The shock wave propagates upstream, leading to cloud shedding and complete sheet extinction at a frequency of $St_1 = 0.12$. The index 1 denotes the most dominant mode as detailed below.

In regime (II), the cavity sheet length is short, $\hat{a}_+ = 0.33$ and 0.24, see Fig. 4 and Table 1, at higher cavitation numbers, $\sigma = 3.0$ and 3.4, respectively. The re-entrant flow dominates the shedding process.

An overview of the SPOD results for $\sigma \in \{1.4, 2.0, 2.2, 3.4\}$ is presented with the SPOD spectrum, the real parts of up to three dominant spatial modes and the Welch PSD of the real part of the time coefficient, cf. Fig. 5. The SPOD spectrum shows the variance of the identified mode pairs against their corresponding frequency as scattered dots. The dot size corresponds to the harmonic correlation of the mode pair, cf. Sieber et al. (2016).

The selected modes are presented with spatial modes from the top and side view, as well as the PSD of the mode coefficient. The window size of the Welch PSD is 512 with 50 % overlap. For clarity, the axis labels and tick labels for the spatial modes have been omitted.

Regime (I) and (II) exhibit a clear dominant first mode with shockwave-driven and re-entrant flow-driven cavitation (Fig. 5a and d). Both operation points in the transition region (Fig. 5b and c) exhibit more complex modes. For instance, mode 3, shown in Fig. 5c, demonstrates asymmetric shedding about the xz-plane, i.e. the midspan line of the hydrofoil, with cloud shedding alternating between the upper and lower sides of the hydrofoil when viewed from the top view. The dominance of the fundamental mode in regimes (I) and (II) is evident from the higher variance K_1 of the most dominant mode 1, as shown in Table 1.

In the transition regime (I)–(II) (Fig. 5b), mode 1 is the mode at the high-frequency band, associated with the re-entrant flow dominated shedding at $St_1 = 0.6$, and mode 2 is at the low-frequency band at $St_2 = 0.14$ associated with shockwave-driven cavitation. The spatial modes differ as well; the spatial wavelength of mode 1 is about 1.5 times greater than that of mode 2. No further analysis is carried out at this point, and only the most important modes for the various regimes are compared. The detailed analysis can be found in Sects. 4.1 to 4.3.

All important quantities and parameters for the five selected operation points can be found in Table 1. The dimensionless sheet length $\hat{a}_+$ which begins at the hydrofoil leading edge and concludes at the point of maximum sheet extension is determined using a deep learning approach, i.e. a modified U-Net (Ronneberger et al. 2015).

In the following subsections, we carry out a detailed analysis of the operation points in Table 1 labelled by an asterisk (*). We focus on the transient analysis of the cavitating flow, using the time coefficients provided by the SPOD and identify the time ranges corresponding to the occurrence of the specific modes. The SPOD findings are compared to the pressure signals and space–time diagrams derived from high-speed recordings.

A significant benefit of SPOD, in contrast to DMD as well as the SPOD variant by Towne et al. (2018), lies in its intrinsic suitability for transient analysis using the SPOD time coefficients. Conducting transient analysis using other methods demands considerably more effort. These methods are primarily employed to identify average flow fields through the analysis of a large volume of data.

A detailed comparison of POD, DFT and SPOD is made in Appendix C for regime (II), since the shedding dynamics are lucid due to its unimodality.

4.1 Regime (I): shockwave-driven cloud cavitation

Regime (I) exhibits a strong periodicity, where shockwaves cause a complete extinction of the cavity. The SPOD spectrum along with the PSD of the transducer is shown in Fig. 6 for $\sigma = 1.4$, where the two first modes are highlighted. The Strouhal number of the first and the second mode is $St_1 = 0.12$ and $St_2 = 0.24$, respectively, which is clearly visible as a dominant peak in the PSD of the pressure signals.

The corresponding variances that can be roughly interpreted as an energy are $K_1 = 47\,\%$ and $K_2 = 10\,\%$, respectively, cf. Sect. 2. SPOD succeeds in identifying the two dominant modes from the high-speed recordings. The second mode is the first harmonic of the fundamental mode 1. Higher harmonics are also visible as peaks in the spectrum.

The corresponding spatial modes $\Psi_{i,j}$, i being the mode number, $j = 1$ and $j = 2$ the real and imaginary parts, respectively, from the side and the top views exhibit more or less the same spatial pattern or have the same wavelength (Fig. 7).

The physical interpretation of the modes is identified from the transient analysis presented in Fig. 8. The first two plots, Fig. 8 a and b, show the real and imaginary parts of the complex time coefficient of the ith mode $\tilde{b}_i$ against the dimensionless time $t_+ := t\,U\,/\,L$, non-dimensionalised by the advection time L/U. The boundaries of the grey-filled area correspond to the envelope of the amplitude of the ith complex time coefficient $|\tilde{b}_i|$.

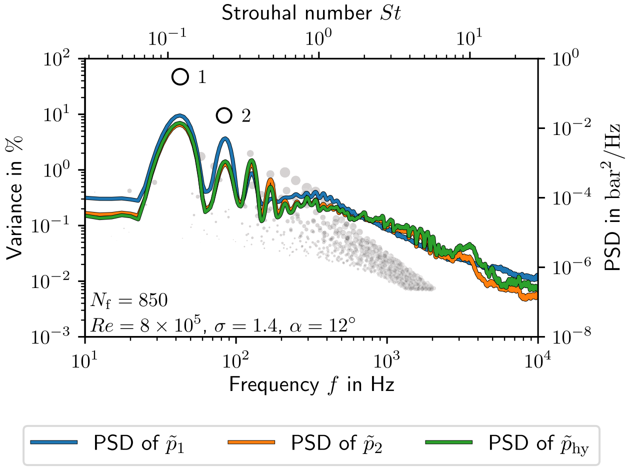

Fig. 6 SPOD spectrum for $\sigma = 1.4$, regime (I): shockwave-driven cloud cavitation, where the variance and the PSD of the three pressure signals $\tilde{p}_1$, $\tilde{p}_2$, $\tilde{p}_\mathrm{hy}$ are plotted against the frequency and the Strouhal number. The first two modes are depicted. A single dot in the SPOD spectrum corresponds to one mode pair and their size is the harmonic correlation between them

Fig. 8c shows the normalised pressure signal $\tilde{p}_1'$ along with the negative normalised greyscale value $-I'$, cf. Barbaca et al. (2019), at positions $x/L = 1.2$, $y/L = 0$ from the top view and $x/L = 1.2$, $z/L = 0$ from the side view, for about 10 cycles.

We decide to plot p_1' rather than p_2', since the correlation between the time coefficient of the second mode with p_1' is higher than its correlation with p_2' (Fig. 10). The mathematical equation to calculate the Pearson correlation coefficients is provided in Appendix B.

We normalise the signals using

$$(\,\cdot\,)' = \frac{(\,\cdot\,) - \overline{(\,\cdot\,)}}{\sigma(\,\cdot\,)}, \tag{13}$$

to make them comparable, $\overline{(\,\cdot\,)}$ being the mean and $\sigma(\,\cdot\,)$ the standard deviation of $(\,\cdot\,)$. The location of the greyscale probes is illustrated in Fig. 9, where the colour of the signal curve (Fig. 8c) matches the colours of the dots indicating where the probes were placed.

A high greyscale value occurs when a cavitation cloud passes, which corresponds to a pressure drop due to the circulation of the cloud. Therefore, we take the negative of the greyscale value to compare both signals. The signals, i.e. $\tilde{p}_1'$ and $-I'$, correlate very well and the cycles are clearly visible, see Fig. 8c.

Fig. 8d shows a space–time diagram from the top view at position a), $y/L = 0$, cf. Fig. 9, where the strong periodic behaviour of shockwave-driven cloud cavitation is apparent.

The cycle starts with the development of a re-entrant flow, which cuts off the sheet at several locations leading to cloud shedding and local peaks in the pressure signal p_1', cf. $t_+ = 38$ to 40 or $t_+ = 47$ to 49 in Fig. 8c, which correlates with the shed clouds in the space–time diagram (Fig. 8d).

Fig. 7 First two spatial SPOD modes for $\sigma = 1.4$, regime (I): shockwave-driven cloud cavitation. Top row: top view, bottom row: side view. $\Psi_{i,j}$ is the spatial mode, where i is the mode number, $j = 1$ and $j = 2$ are the real and imaginary parts, respectively

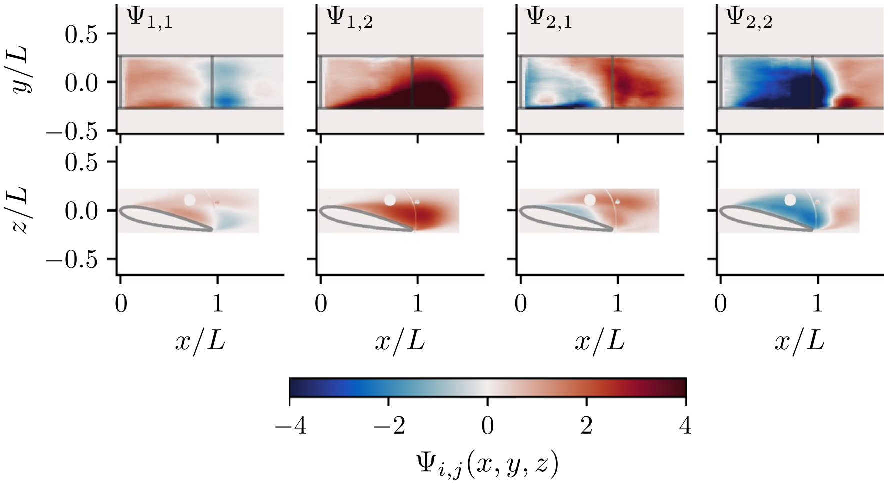

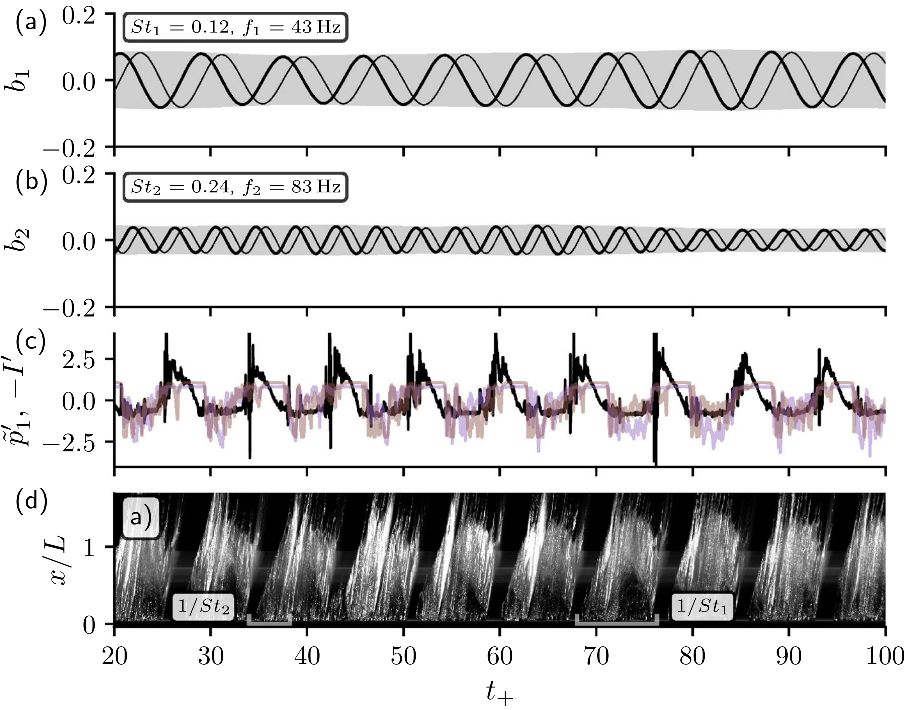

Fig. 8 Time series for $\sigma = 1.4$, regime (I); **a** and **b** are the time coefficients of the first and second mode, where the thick line (▬) is the real part and the thin line (—) the imaginary part. The boundaries of the grey-filled area correspond to the envelope of the time coefficient, i.e. the amplitude. **c** shows the normalised pressure signal $\tilde{p}'_1$ and negative normalised greyscale values $-I'$ at positions $x/L = 1.2$, $y/L = 0$ and $x/L = 1.2$, $z/L = 0$. **d** is a space–time diagram at $y/L = 0$, a) in Fig. 9, where the flow is from bottom to top. The periods of the two first modes are annotated within the plot. The time is non-dimensionalised and $\Delta t_+ = 80$ corresponds to 230 ms

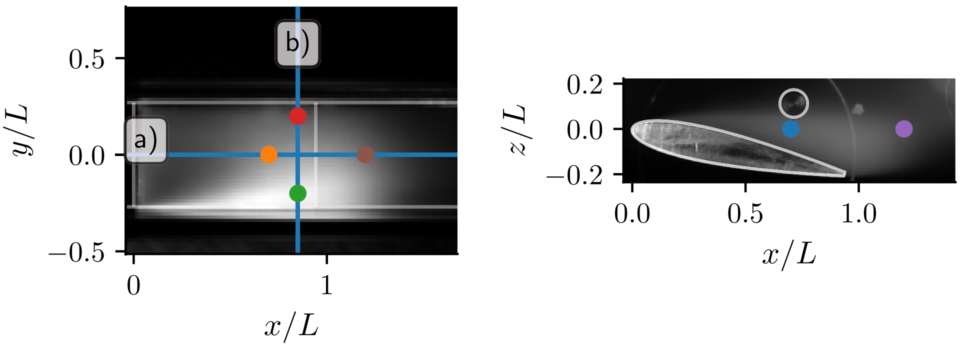

Fig. 9 Left: top view, right: side view. The coloured dots are the points where the time series of the greyscale values are taken, the blue lines denoted by a) and b) are the cuts through the frame, from where the space–time diagrams are created. The positions are $x/L = 0.7$, $z/L = 0$ for ●; $x/L = 0.7$, $y/L = 0$ for ●; $x/L = 0.85$, $y/L = -0.2$ for ●; $x/L = 0.85$, $y/L = 0.2$ for ●; $x/L = 1.2$, $y/L = 0$ for ●; $x/L = 1.2$, $z/L = 0$ for ●. The cuts for the space–time diagrams are at the positions $y/L = 0$ for a), $x/L = 0.85$ for b)

The intensity of this phenomenon varies from cycle to cycle depending on the cloud collapse energy. The number of peaks caused by a prior cloud shedding and subsequent collapse can vary between one or two peaks in the pressure signal p'_1 (Fig. 8c), depending on the number of shed clouds and collapses. The development of a re-entrant flow in shockwave-driven cloud cavitation is also reported by Venning et al. (2022), Zhang et al. (2022), Vaca-Revelo and Gnanaskandan (2023), and Bhatt et al. (2023).

After the re-entrant flow occurrence, the sheet length reaches a maximum value of about $\hat{a}_+ = 1.43$ and a shock wave develops, leading to a complete extinction of the sheet (Fig. 8d). One whole cycle is shown in detail in Fig. 11. The cavity sheet begins to grow at $t_+ = 68.5$, as indicated by the blue dashed line. The re-entrant flow develops and stagnates around $x/L = 0.2$ to 0.3, before accelerating upstream, leading to multiple cloud shedding events. The first large-scale cloud shedding is marked by the orange dashed line. As the re-entrant flow reaches the leading edge of the cavity, it triggers a second cloud shedding event, also denoted by the orange dashed line. The cavity sheet then rapidly regrows to its maximum length, after which a condensation shockwave forms, indicated by the red dashed line. Although the initial stage of shockwave formation is difficult to discern in the space–time

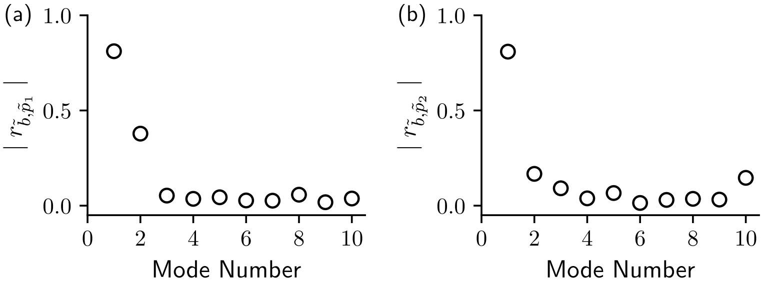

Fig. 10 Absolute value of the Pearson correlation coefficient $|r_{\tilde{b},\tilde{p}}|$ for $\sigma = 1.4$, regime (I), between the complex time coefficient $\tilde{b}(t)$ and the pressure signal **a** $\tilde{p}_1(t)$ and **b** $\tilde{p}_2(t)$, respectively

plot, it becomes more apparent in supplementary movie 7, where these flow features are highlighted in the same colours. As the condensation shockwave propagates upstream, the sheet is disrupted at several locations. By $t_+ = 76$, cavitation around the hydrofoil is completely extinguished, and the cycle restarts, see the corresponding supplementary movie 7 to Fig. 11.

The velocity of the shock front is determined from the slope of the shock wave curve as $U_\mathrm{s} = 13.1\,\mathrm{m/s}$ or $U_\mathrm{s}/U = 0.81$, which is consistent with the values provided by Bhatt et al. (2023) for a NACA 0015 and an incidence of 10°.

The first mode with a Strouhal number of $St_1 = 0.12$ represents the main dominant cycle, where its period is annotated as $1/St_1$ in Fig. 8d. This mode is dominant throughout the entire experiment, concluded by a high absolute value of its complex time coefficient $|\tilde{b}_1|$. However, between $t_+ = 40$ and 45 there is no complete extinction of the sheet, leading to a small reduction in the absolute value of the time coefficient (Fig. 8a).

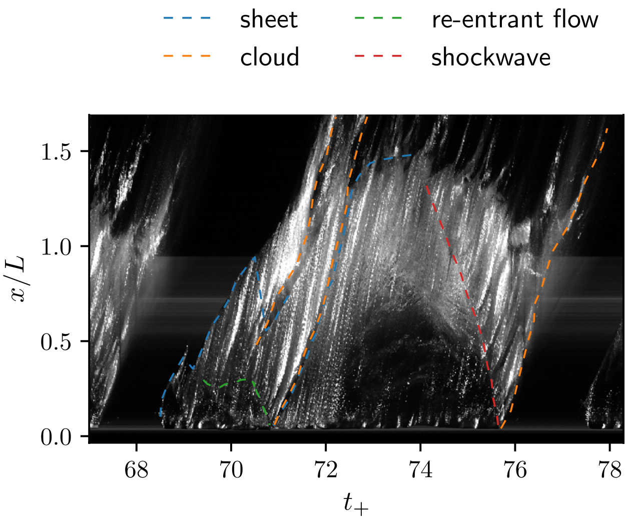

Fig. 11 Detailed view of one cycle for $\sigma = 1.4$, regime (I): Shockwave-driven cloud cavitation. The cycle starts with no cavitation visible at the leading edge at $t_+ = 68$. The sheet starts to grow denoted by the blue path. The re-entrant flow develops, stagnates and accelerates upstream, denoted by the green path and disrupts the cavity at multiple location. Two large-scale cloud shedding events are denoted by the orange path. When the sheet reaches its maximum value, the shockwave, denoted by the red path, develops, leading to a complete extinction of the cavity. Supplementary Movie 7, which we have provided, shows the flow features in the same colours as presented here. This cycle is also visualised in the supplementary movies 1 and 2

The second mode, $St_2 = 0.24$, represents the preceding cycle initiated by the re-entrant flow as described above. Higher harmonics are often ignored and considered artefacts, as in the Fourier transformation for non-sinusoidal signals, in rebuilding the signal. However, the transient analysis reveals that the first harmonic, or mode 2, provides crucial insights into the cycle-to-cycle variation of the fundamental mode 1 as detailed next.

The period of the harmonic $1/St_2$ is also annotated in Fig. 8d. As previously mentioned, mode 2 characterises the intensity of the preceding cycle in which the re-entrant flow occurs. Its intensity can be correlated with the small peaks in p_1' during the shedding and collapse of the re-entrant flow-induced clouds, cf. around $t_+ = 39$, 49 and 65 (Fig. 8c and d). If the preceding cycle is strong, the absolute value of the time coefficient of the second mode exhibits a higher value (Fig. 8b).

From $t_+ = 85$ to 95 the small peaks in the pressure $\tilde{p}_1'$ are weaker, which results in a decrease in the amplitude $|\tilde{b}_2|$.

The reason for the small peaks correlating with the amplitude of mode 2 is that the pressure signal p_1' is similar to a sawtooth waveform $t_+ = 20$ to 80, whereas the two cycles for $t_+ > 80$ are more similar to a sine wave (Fig. 8c). This reduces the amplitude in mode 2 and shifts the phase of mode 2 relative to mode 1. Ignoring the harmonic would leave this cycle-to-cycle variation undetected.

The phenomenon described above displays a highly intermittent behaviour, as the prior cycle does not consistently occur at twice the frequency of the fundamental mode, in this case mode 1. This intermittency is evident in the cycle-to-cycle variations presented in Fig. 8d. A similar pattern is observed at the operating point $\sigma = 1.6$ (not shown). Additionally, this mode 2 contains the necessary harmonics to reconstruct the non-sinusoidal signal.

A reconstruction of the flow field using modes 1 and 2 and a simultaneous visualisation of the time coefficients for the cycle in Fig. 11 are provided as supplementary movies 1 and 2, respectively.

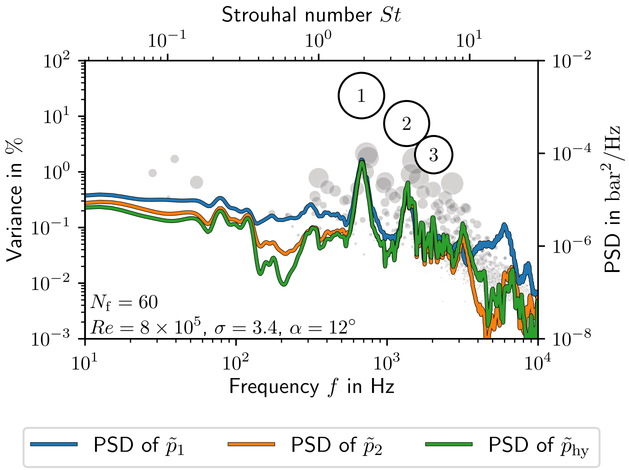

Fig. 12 SPOD spectrum for $\sigma = 3.4$, regime (II): re-entrant flow-driven cloud cavitation, where the variance and the PSD of the three pressure signals $\tilde{p}_1$, $\tilde{p}_2$, $\tilde{p}_\mathrm{hy}$ are plotted against the frequency and the Strouhal number. The first three modes are depicted. A single dot in the SPOD spectrum corresponds to one mode pair and their size is the harmonic correlation between them

4.2 Regime (II): re-entrant flow-driven cloud cavitation

Regime (II) exhibits unimodal behaviour with the re-entrant flow being the dominant mechanism for the well-defined temporal periodicity. The detailed analysis is conducted for a cavitation number of $\sigma = 3.4$.

The SPOD spectrum of re-entrant flow-driven cavitation exhibits three dominant modes, where the Strouhal numbers are $St_1 = 1.92$, $St_2 = 3.83$ and $St_3 = 5.78$, respectively (Fig. 12). The second and third modes are the first and second harmonic of the fundamental mode 1, and therefore, their corresponding frequency is twice and triple the fundamental frequency. The modes match the peaks observed in the pressure signals as shown in Fig. 12.

The sum of the variances of the first three modes is $K = 33\,\%$, being less than for shockwave-driven cloud cavitation (Sect. 4.1), where the sum of the variances of the first two modes reach $K = 57\,\%$. It can be concluded that shockwave-driven cavitation is more regular and therefore contains more energy in the fundamental mode 1 and its harmonic compared to re-entrant flow-driven cloud cavitation.

The wavelengths of the corresponding second and third spatial modes or the first and second harmonic of the fundamental mode 1 exhibit half and one-third of the wavelength of the fundamental mode, respectively (Fig. 13).

The fundamental shedding is not sinusoidal; thus, the harmonics occur to rebuild the signal. That becomes more clear in the Lissajous curves, where there is a constant phase difference between the fundamental mode and the second and third modes (Fig. 26d–f).

The absolute values of the time coefficients $|\tilde{b}_i|$ decrease and increase simultaneously for all three modes (Fig. 14a–c), in contrast to the higher harmonic mode in Sect. 4.1 for shockwave-driven cloud cavitation (Fig. 8). Again, the higher harmonics are not artefacts but rather attempts to reconstruct a signal that

Fig. 13 First three spatial SPOD modes for $\sigma = 3.4$, regime (II): re-entrant flow-driven cloud cavitation. Top row: top view, bottom row: side view. $\Psi_{i,j}$ is the spatial mode where i is the mode number, $j = 1$ and $j = 2$ are the real and imaginary parts, respectively.

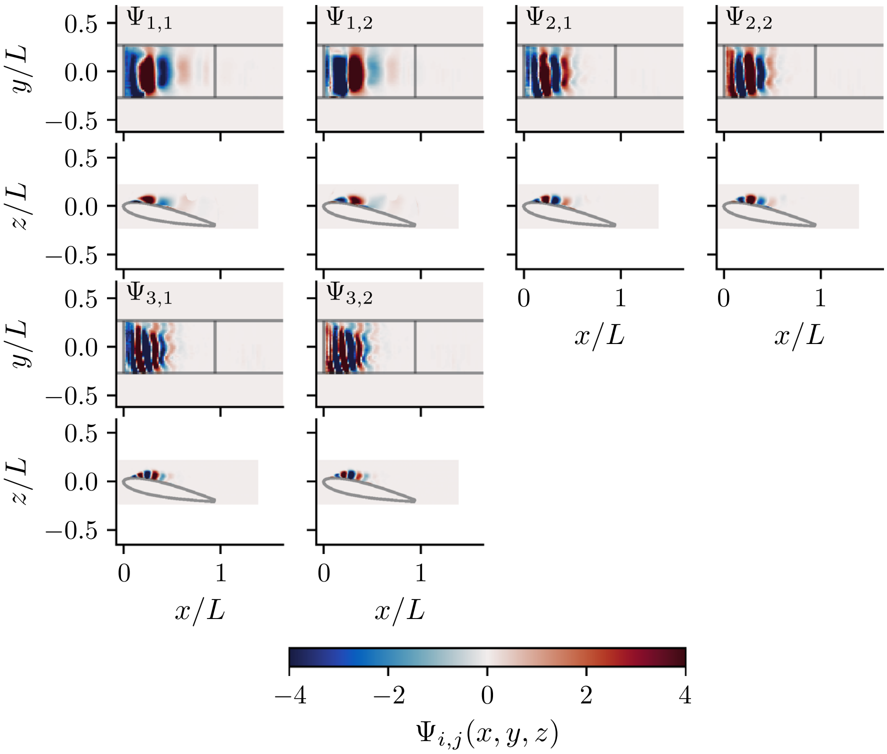

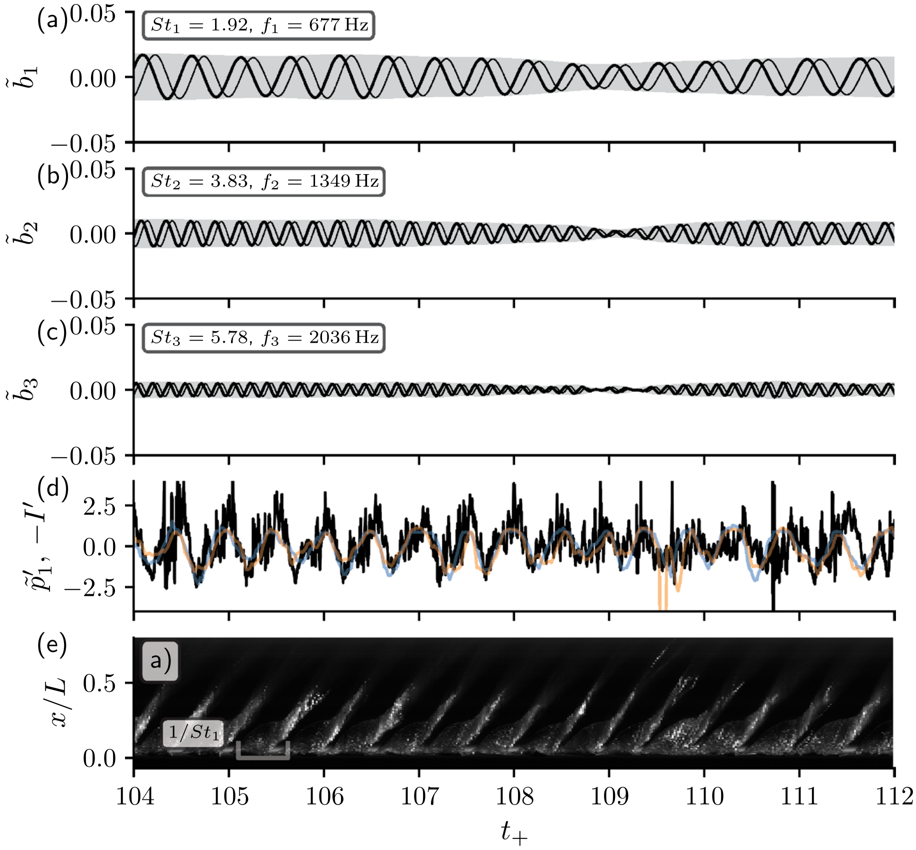

Fig. 14 Time series for $\sigma = 3.4$, regime (II); **a**–**c** are the time coefficients of the first, second and third modes, where the thick line (━━) is the real part and the thin line (——) the imaginary part. The boundaries of the grey-filled area correspond to the envelope of the time coefficient, i.e. the amplitude. **d** shows the normalised pressure signal $\tilde{p}_1'$ and negative normalised greyscale values $-I'$ at positions $x/L = 0.7$, $y/L = 0$ and $x/L = 0.7$, $z/L = 0$. **e** is a space–time diagram at $y/L = 0$, a) in Fig. 9, where the flow is from bottom to top. The period $1/St_1$ of the fundamental mode is annotated within the plot. The time is non-dimensionalised and $\Delta t_+ = 8$ corresponds to 23 ms. Two supplementary movies 3 and 4 are provided to reconstruct and visualise the mode

is not sinusoidal. This is elucidated in the supplementary movie 3 where the original flow is reconstructed using the first, the first two and the first three modes.

Between $t_+ = 108$ and 110, the periodicity is disturbed, indicated by low amplitudes of the time coefficients. This is also visible in the pressure signal $\tilde{p}_1$ and the greyscale signal I (Fig. 14d), as well as in the space–time diagram (Fig. 14e). The non-dimensionalised period, which corresponds to the reciprocal of the Strouhal number, $1/St_1$, is depicted as a scale in Fig. 14e. This scale highlights that the primary cloud shedding corresponds to the fundamental mode. The supplementary movie 4 is provided where the time coefficients are plotted simultaneously to the high-speed recordings.

The detailed space–time diagram shows the re-entrant flow-driven cavitation cloud shedding (Fig. 15). The corresponding movie 8, with highlighted colours, is also provided. The cycle starts with a growing cavity sheet and reaches a maximum value of $\hat{a}_+ = 0.24$. The re-entrant flow develops and cuts off the cavity sheet near the leading edge. In contrast to shockwave-driven cavitation, the sheet is not fully extincted. The sheet is U-shaped during its growth process due to the influence of the walls, rather than being a straight line as in regime (I).

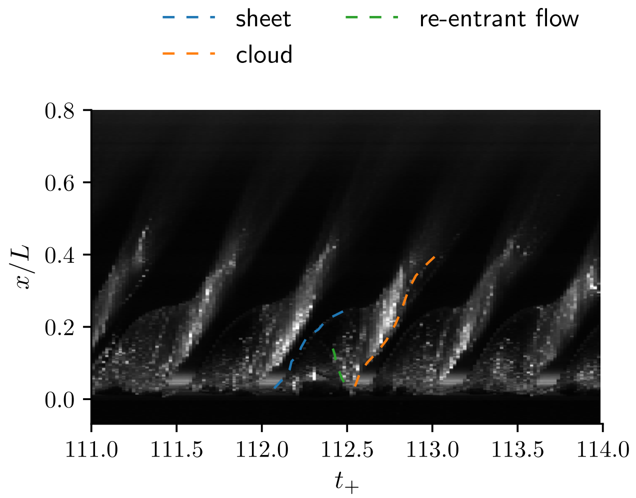

Fig. 15 Detailed view of the space–time diagram for $\sigma = 3.4$, regime (II): re-entrant flow-driven cloud cavitation. The cycle starts with a growing cavity sheet and reaches the maximum sheet length of $\hat{a}_+ = 0.24$. The re-entrant flow develops and cuts off the sheet at the cavity leading edge. In contrast to shockwave-driven cavitation, the sheet is not fully extincted. The frequency of this periodic process is $St_1 = 1.92$ or $f_1 = 677$ Hz. Supplementary movie 8, which we have provided, shows the flow features in the same colours as presented here

Tracking the re-entrant flow velocity in the available data is challenging; however, we identified a time instance where it can be observed, as shown in Fig. 15, where it is highlighted in green at $x/L \approx 0.15$. Its upstream velocity can be roughly estimated as $U_{\mathrm{rf}}/U = 1.14$.

We can also estimate the re-entrant flow velocity based on the entire cloud shedding period. The Strouhal number, based on the maximum sheet length, $St_{\hat{a}}$, is constant and can be calculated as

$$St_{\hat{a}} := \frac{f\hat{a}}{U} \approx 0.42 \tag{14}$$

in our experiments, cf. Hatzissawidis et al. (2025). This is consistent with values reported in the literature, where they vary from 0.25 to 0.4, cf. Kawanami et al. (1997); Callenaere et al. (2001); Arndt (2012).

The re-entrant flow velocity is $U_{\mathrm{rf}} = \hat{a}/T_{\mathrm{rf}}$, with T_{rf} being the time it takes for the re-entrant flow to progress from its initial appearance to reaching the leading edge. From Keil (2014), we can assume $T_{\mathrm{rf}} \approx 1/3\,T$, where T is the period of the whole cycle, i.e. $T = 1/f$. Solving $U_{\mathrm{rf}} \approx 3\,\hat{a}f$ for f and substituting into Eq. (14), we obtain $U_{\mathrm{rf}}/U \approx 1.26$, which is consistent with the previously calculated value.

In the literature, values ranging from 0.5 to 1.1 are reported for a convex lower surface, cf. Pham et al. (1999), and 0.5 of the velocity at the minimum cross-sectional area for a diverging step, cf. Callenaere et al. (2001). Recently, Bhatt et al. (2023) found values between 0.41 and 0.75 of the free-stream velocity around a NACA0015 hydrofoil.

It should be noted that, as in internal flows, the velocity at the minimum cross-sectional area does not match our free-stream velocity due to blockage effects and flow acceleration around the hydrofoil. Consequently, the characteristic velocity in our experiment is underestimated and not directly comparable to studies about internal flows. However, our approximate calculations indicate that the ratio of re-entrant flow velocity to free-stream velocity is slightly larger than unity.

In comparison with the velocities calculated for shockwaves in Sect. 4.1, re-entrant flow velocities are of the same order of magnitude. However, the entire shockwave-driven cycle, as illustrated in Fig. 11, operates on a longer timescale due to the distinct nature of the mechanism. Prior to the shockwave, cloud shedding events and the regrowth of the cavity occur. The shockwave, which leads to the complete extinction of the cavity sheet, only occurs after the sheet has reached its maximum extent following regrowth, and it occupies a significantly smaller portion of the overall cycle time.

4.3 Transition regime (I) to (II)

The transition regime (I)-(II) is defined for $1.8 < \sigma < 2.5$, where the lower-frequency band, which does not depend on the cavitation number, and the high-frequency band, which depends on the cavitation number, occur simultaneously. We analyse the operation point $\sigma = 2.2$, where we select the first five dominant modes (Fig. 16). The SPOD mode frequencies and the peaks from the pressure transducers are again in good agreement. The corresponding spatial modes are shown in Fig. 17.

This operation point exhibits a more complex shedding behaviour characterised by multiple dominant modes that occur intermittently and simultaneously. The fundamental mode 1 is on the high-frequency band at $St_1 = 0.66$, which is associated with re-entrant flow. The mode that is associated with shockwaves on the low-frequency band is mode 4 with a Strouhal number of $St_4 = 0.17$.

To analyse and understand the physics of the modes, we use the time coefficients to identify at which times the modes occur, since they are intermittent. Fig. 18 shows the time-dependent Strouhal number against the dimensionless time t_+. The time-dependent Strouhal number is calculated using the real and imaginary parts of the complex SPOD time coefficients $\tilde{b}(t) = b_i(t) + \mathrm{i}\, b_j(t)\tilde{b}(t)$. $b_i(t)$ and $b_j(t)$ denote the real and the imaginary part, respectively. The frequency can be computed as the gradient of the angle of the complex time coefficient $\tilde{b}(t)$,

$$\varphi(t) = \arctan \frac{b_j(t)}{b_i(t)}, \tag{15}$$

as $f(t) = \partial\varphi(t)/\partial t$ or $St(t) = f(t)\,L/U$. The line thickness and colour map in Fig. 18 represent the absolute value or amplitude of $\tilde{b}(t)$, which describes the dominance of the mode at time t. Using this plot, it is possible to get an information of the frequency $f(t)$ over time, similar to a wavelet

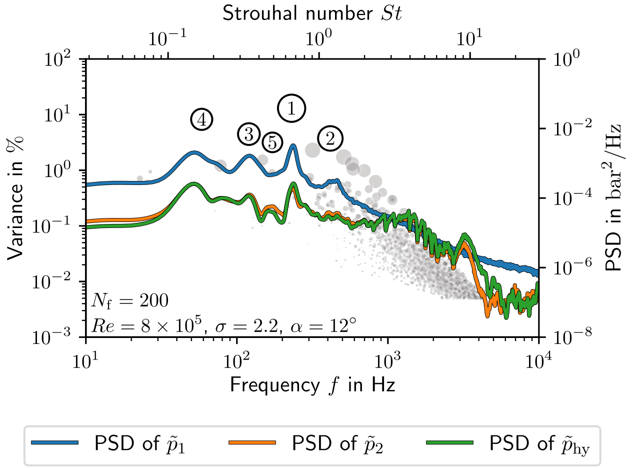

Fig. 16 SPOD spectrum for $\sigma = 2.2$, transition regime (I)–(II): The variance and the PSD of the three pressure signals $\tilde{p}_1$, $\tilde{p}_2$, $\tilde{p}_{\mathrm{hy}}$ are plotted against the frequency and the Strouhal number. The first five modes are depicted. A single dot in the SPOD spectrum corresponds to one mode pair, and their size is the harmonic correlation between them

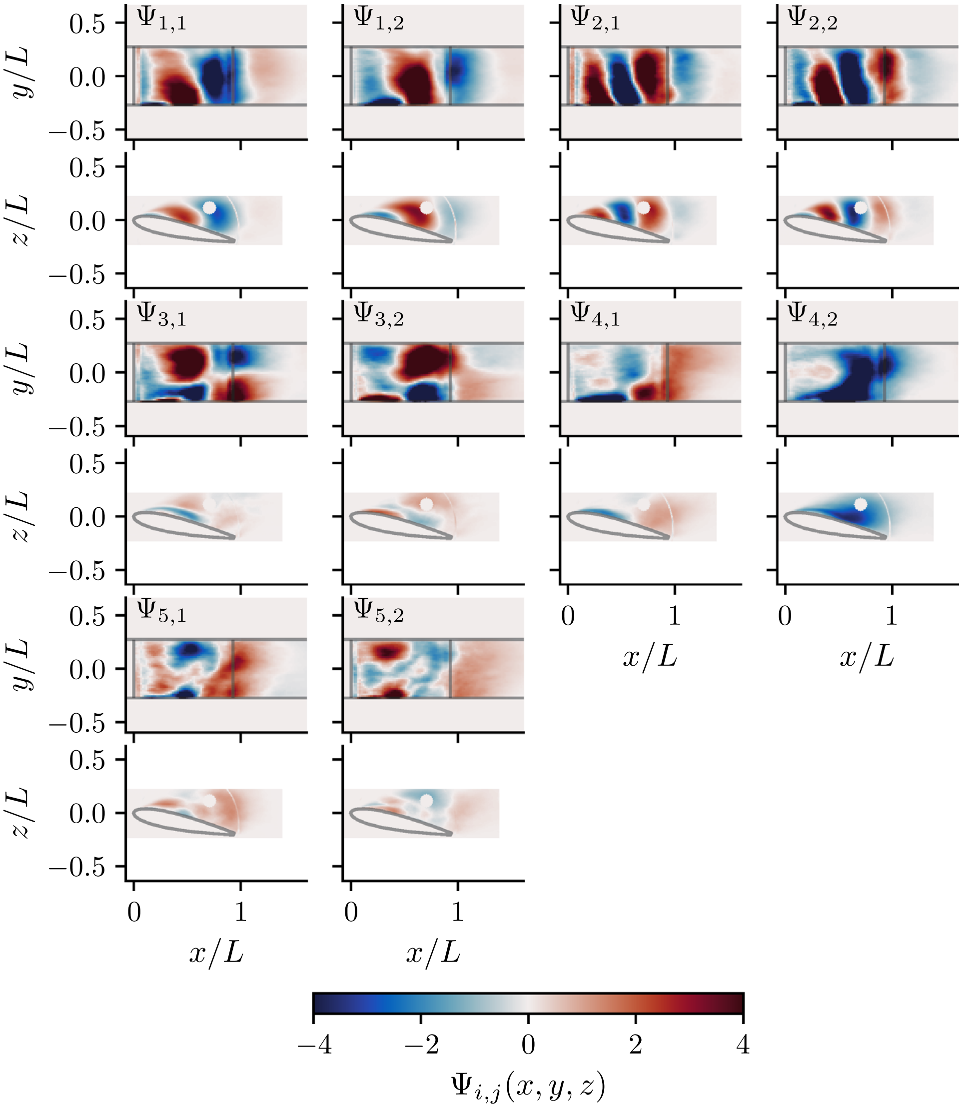

Fig. 17 First five spatial SPOD modes for $\sigma = 2.2$, transition regime (I)–(II): Top row: top view, bottom row: side view. $\Psi_{i,j}$ is the spatial mode where i is the mode number, $j = 1$ and $j = 2$ are the real and imaginary parts, respectively

transformation. Thus, it allows to identify the time ranges where a specific mode occurs.

We depict modes 1 and 2 in the range $120 < t_+ < 150$, denoted by the grey area in Fig. 18a and b, for a detailed analysis in Fig. 19. These modes are associated with the re-entrant flow.

The absolute value of the time coefficient $\tilde{b}_1$ is high for $128 < t_+ < 135$ and $140 < t_+ < 150$ (Fig. 19a), whereas a high absolute value of $\tilde{b}_2$ can be observed within the range $124 < t_+ < 128$ and $136 < t_+ < 140$ (Fig. 19b), concurrent with a low value of $\tilde{b}_1$. Mode 2 differentiates itself uniquely in the space–time diagram for the mentioned time ranges, as annotated in Fig. 19d.

In the time ranges $129 < t_+ < 135$ and $140 < t_+ < 150$, the mode 2 also exhibits a high value. This corresponds to the harmonic amount in mode 2, which follows strictly the fundamental mode 1. We can conclude that mode 2 is not just a higher harmonic of mode 1, but a separate mode, clearly visible in the space–time diagram. For the reconstruction of the flow field, we refer to the supplementary movie 5.

Mode 3 is an asymmetric mode (Fig. 17), exhibiting asymmetric cloud shedding about the *xz*-plane, i.e. the midspan line of the hydrofoil. This mode is visible within the time range $35 < t_+ < 65$, cf. Fig. 18c, and exhibits a Strouhal number of $St_3 = 0.34$, which is about half of the frequency of mode 1. Barbaca et al. (2019) also observed asymmetric modes about a two-dimensional geometry using POD.

Mode 3 is strongly intermittent; a few cycles are visible in the space–time diagram (Fig. 20e), at a vertical position b) in the wake, $x/L = 0.85$, see Fig. 9 for the locations of the space–time diagram. One cycle is annotated as $1/St_3$, where the shed cloud is firstly shed on the upper side of the midspan.

The time coefficient $\tilde{b}_3$ shows that four cycles are present within the time range of $42 < t_+ < 57$, which are visible as

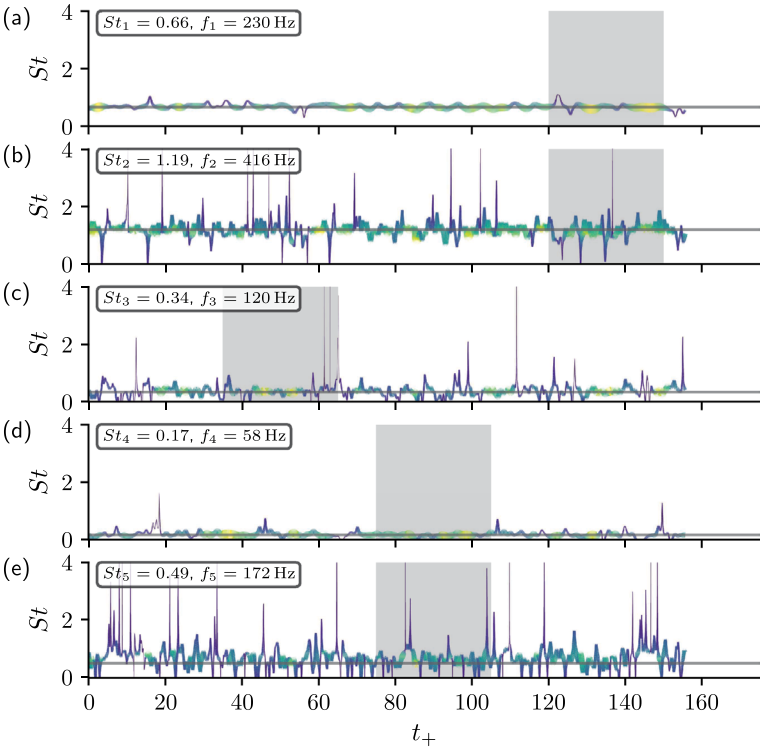

Fig. 18 Time series for $\sigma = 2.2$, transition regime (I)–(II). The plots show the gradient of the angle of the complex time coefficient of the first five modes, which is equal to the frequency or Strouhal number. The colour and line thickness correspond to the absolute value of the complex time coefficient. The grey-filled areas are the time patches depicted for the detailed analysis below, since the modes exhibit high absolute values there. The detailed views of these time patches are shown in Figs. 19, 20 and 21. The time is non-dimensionalised and the physical time for the whole measurement is 444.5 ms.

asymmetric shedding in the space–time diagram (Fig. 20e). Mode 1 occurs simultaneously (Fig. 20a), annotated in the space–time diagram (Fig. 20d). Hence, the shedding in the fundamental mode is asymmetric. This phenomenon can be reconstructed through the superposition of modes 1 and 3. After asymmetric mode 3 disappears, the intensity of mode 1 increases for $t_+ > 57$ (Fig. 20a and b). We refer to the supplementary movie 6, where the flow field is shown

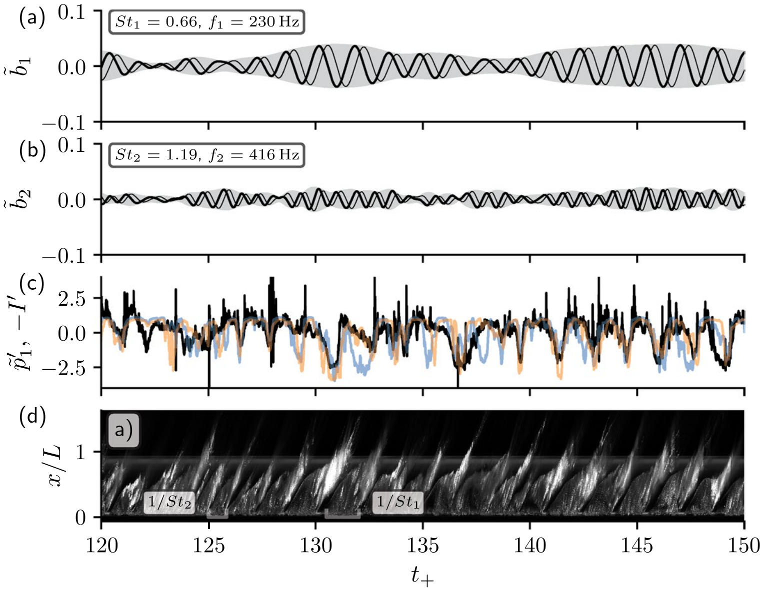

Fig. 19 Time series for $\sigma = 2.2$, transition regime (I)–(II), for modes 1 and 2; **a–b** are the time coefficients of the first and second mode, where the thick line (▬▬) is the real part and the thin line (——) the imaginary part. The boundaries of the grey-filled area correspond to the envelope of the time coefficient, i.e. the amplitude. **c** shows the normalised pressure signal $\tilde{p}_1'$ and negative normalised greyscale values $-I'$ at positions $x/L = 0.7$, $y/L = 0$ and $x/L = 0.7$, $z/L = 0$. **d** is a space–time diagram at $y/L = 0$, a) in Fig. 9, where the flow is from bottom to top. The periods of modes 1 and 2 are annotated within the plot. The time is non-dimensionalised and $\Delta t_+ = 30$ corresponds to 87 ms. The supplementary movie 5 is available where the flow field is reconstructed using modes 1-5

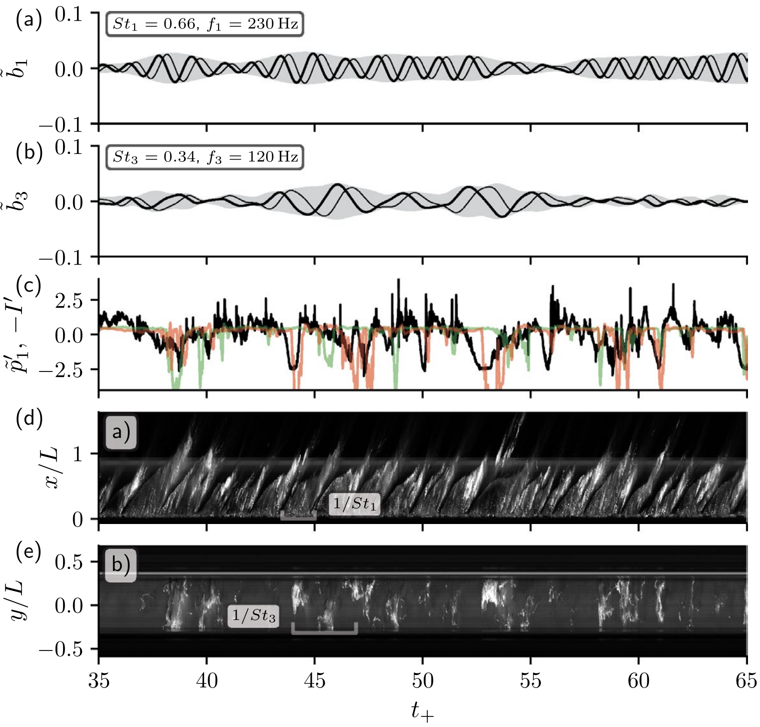

Fig. 20 Time series for $\sigma = 2.2$, transition regime (I)–(II), for the fundamental mode 1 and the asymmetric mode 3; **a** shows the time coefficient of the first mode. **b** shows the time coefficient of the third mode, where the thick line (▬▬) is the real part and the thin line (——) the imaginary part. The boundary of the grey-filled area correspond to the envelope of the time coefficient, i.e. the amplitude. **c** shows the normalised pressure signal $\tilde{p}_1'$ and negative normalised greyscale values $-I'$ at positions $x/L = 0.85$, $y/L = 0.2$ and $x/L = 0.85$, $y/L = -0.2$. **d** and **e** are the space–time diagram at $y/L = 0$ and $x/L = 0.85$, a) and b) in Fig. 9, respectively. The periods of both modes 1 and 3 are annotated within the plot. The time is non-dimensionalised and $\Delta t_+ = 30$ corresponds to 87 ms. The supplementary movie 6 is available to visualise the asymmetric shedding

simultaneously to the time coefficients for the time range in Fig. 20.

Since the correlation between $\tilde{p}_1$ and the time coefficient of mode 3, $\tilde{b}_3$, is high (Fig. 22), we plot $\tilde{p}_1$ rather than $\tilde{p}_2$, together with the greyscale value at $x/L = 0.85$, $y/L = 0.2$ and $y/L = -0.2$, cf. Fig. 9, to illustrate the asymmetric shedding. As expected, the values alternately decrease and increase.

As mentioned above, mode 4 is on the low-frequency band (Fig. 3). The corresponding cycle is visible from $94 < t_+ < 100$ (Fig. 21e and f). The cycle includes two cloud sheddings associated with smaller cavity sheet lengths and finally two with larger sheet lengths, where the latter is shockwave-driven, leading to complete sheet extinction at $t_+ \approx 99.5$. However, differentiating between the two shedding mechanisms, re-entrant flow and shockwaves, from high-speed recordings poses a non-trivial challenge.

Mode 4 is a low-frequency mode that contains four cloud shedding cycles, see Fig. 17 for the spatial structure. The large wavelength of that mode is visible from the side view of the spatial mode, which is similar to Fig. 7, where the shockwave-driven mode is split into two modes.

During mode 4's activity, the fundamental mode 1 is active as well, indicating a fluid dynamic relation of both modes (Fig. 21a and b).

Occasionally, mode 5 occurs intermittently (Fig. 21c), which has a lower-frequency than fundamental mode 1 (Fig. 21e). A superposition of modes 1, 4 and 5 allows for the reconstruction of the shedding consisting of various individual cycles as it is shown in the space–time diagram (Fig. 21e). Mode 4 undergoes a transition to the shockwave-driven cycle as discussed in Sect. 4.1.

5 Conclusion

The data-driven technique SPOD was applied to analyse high-speed recordings from cavitating flow fields obtaining spatial and temporal information, and its benefits were demonstrated on experimental data of cloud cavitation about a NACA 0015 hydrofoil. Since dynamics in cavitation can occur simultaneously or exclusively, i.e. intermittently, classical approaches such as POD or DMD fail to decompose

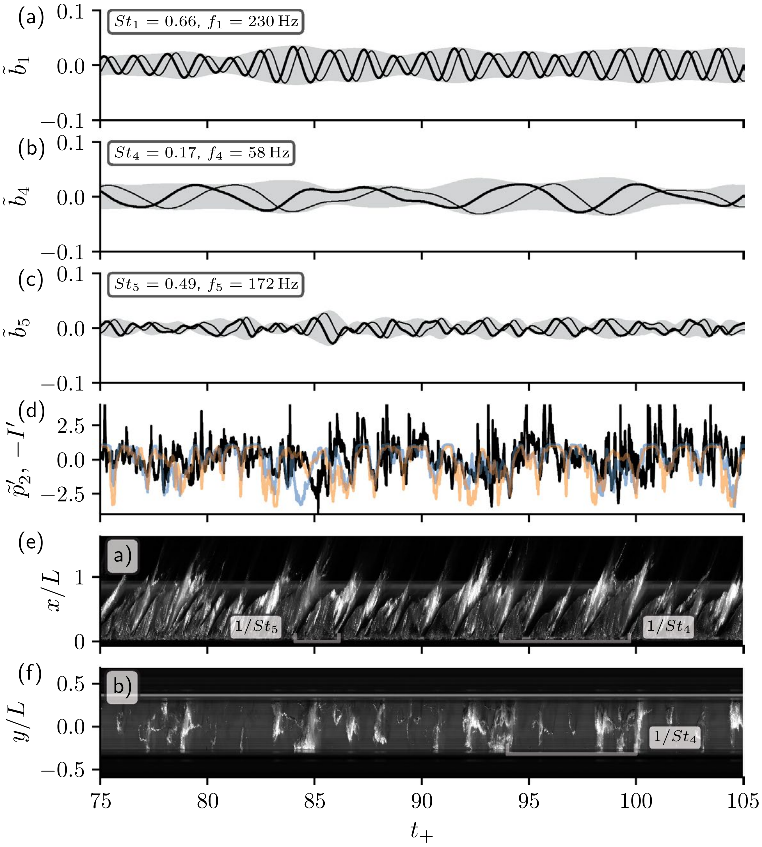

Fig. 21 Time series for $\sigma = 2.2$, transition regime (I)–(II), for modes 1, 4 and 5; **a**–**c** are the time coefficients of the first, fourth and fifth modes, where the thick line (——) is the real part and the thin line (——) the imaginary part. The boundaries of the grey-filled area correspond to the envelope of the time coefficient, i.e. the amplitude. **d** shows the normalised pressure signal $\tilde{p}_2'$ and negative normalised greyscale values $-I'$ at positions $x/L = 0.7$, $y/L = 0$ and $x/L = 0.7$, $z/L = 0$. **e** and **f** are the space–time diagrams at $y/L = 0$ and $x/L = 0.85$, a) and b) in Fig. 9, respectively. The period of mode 4 and 5 is annotated within the plot. The time is non-dimensionalised and $\Delta t_+ = 30$ corresponds to 87 ms.

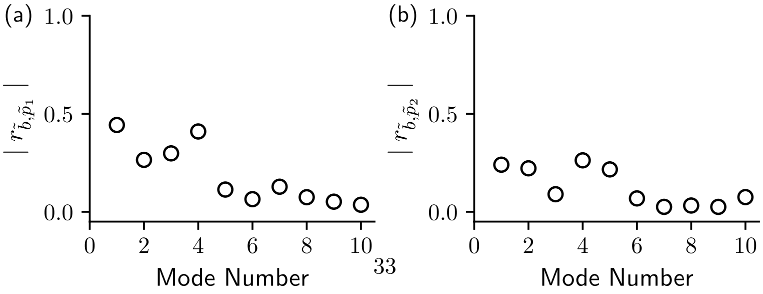

Fig. 22 Absolute value of Pearson correlation coefficient $|r_{\tilde{b},\tilde{p}}|$ for $\sigma = 2.2$, transition regime (I)-(II), between the complex time coefficient $\tilde{b}(t)$ and the pressure signal **a** $\tilde{p}_1(t)$ and **b** $\tilde{p}_2(t)$, respectively

the data into meaningful modes, hindering a physical interpretation.

High-speed recordings with a dual-camera system were obtained for a fixed Reynolds number $Re = 8 \times 10^5$ and incidence $\alpha = 12°$ for a range of cavitation numbers σ, covering cavitation regimes between supercavitation and no cavitation. Simultaneous acoustic signals were obtained to compare and validate the SPOD results.

SPOD enables the identification of the dominant modes, allowing variations in frequency contrary to DFT/DMD, and transforming the POD to meaningful dynamics, Sieber et al. (2016), and physically interpretable modes. Clarity on this matter emerges through the SPOD modes and the examination of the Lissajous figures, where the time coefficients are plotted against each other.

The intrinsic capability of SPOD to conduct a transient analysis presents a significant advantage compared to SPOD by Towne et al. (2018) and DMD, where performing a transient analysis demands considerable effort.

From the time coefficients, it is also possible to determine the variance of the frequency, that is, the variation of the frequency over time, giving a mean and a standard deviation. Since the time coefficients are linked through a harmonic correlation to each other, we obtain a complex time coefficient split into a real and imaginary parts. The derivative of the phase between them equals the frequency. Hence, we obtain a frequency *f*(*t*) over time and a corresponding absolute value of the complex time coefficient, which leads to the same information as a wavelet analysis.

A Welch spectrogram, PSD over σ and *St*, from the high-frequency pressure transducer was determined to acquire an overview of the frequencies that occur. Two predominant frequency bands were identified; one depends on the cavitation number, while the other remains independent of it. Three regimes were defined: (I) shockwave-driven cloud cavitation, (II) re-entrant flow-driven cloud cavitation and (III) sheet cavitation. We focused on regime (I), (II) and the transition regime (I)-(II).

Regime (I) exhibits a strong periodicity, where a re-entrant flow occurs, first leading to occasional and incomplete shedding. The behaviour of the re-entrant flow and the prior cloud shedding shows significant cycle-to-cycle variation. After reaching a maximum sheet length, a shock wave propagates upstream, leading to a complete extinction of the sheet. SPOD was able to identify the entire cycle as the fundamental mode 1. The preceding cycle due to the re-entrant flow mechanism was identified as the harmonic mode 2 with varying intensity depending on the re-entrant flow mechanisms. If this mode were ignored and defined as an artefact, the cycle-to-cycle variation in regime (I) would remain undetected.

Regime (II) is re-entrant flow-driven, exhibiting a well-defined periodicity, where a re-entrant flow develops and reaches the cavity leading edge, resulting in cavity pinch-off. This main shedding cycle is divided into a fundamental mode and higher harmonics to reconstruct the original flow field, which does not display a sinusoidal waveform, akin to the role of higher harmonics in a Fourier transformation for non-sinusoidal signals. In contrast to the harmonic in regime (I), the harmonics in regime (II) follow strictly the fundamental mode 1. SPOD successfully shows the amplitude variation of the re-entrant flow-driven cloud shedding.

The characteristic timescales of the re-entrant flow and the shockwave are of the same order, with the re-entrant flow exhibiting slightly higher velocities. However, the overall period of a shockwave-driven cycle in regime (I) is significantly longer than that of the re-entrant flow-driven cloud cavitation cycle in regime (II). This occurs because the mechanisms involved in shockwave-driven cloud cavitation are more complex, involving the development of the re-entrant flow, which triggers prior cloud shedding and rapid regrowth of the cavity sheet. The shockwave develops once the sheet reaches its maximum extent, leading to the complete collapse of the sheet.

In the transition regime (I)-(II), the modes occur simultaneously as well as intermittently, which was identified by the SPOD. The transition from regime (I) to regime (II) occurs smoothly, with shockwaves becoming increasingly dominant as the cavitation number decreases. At about $\sigma = 1.8$ the high-frequency band, associated with re-entrant flow-driven cloud cavitation vanish when the maximum sheet length reaches the trailing edge of the hydrofoil, cf. Hatzissawidis et al. (2025). SPOD is capable of capturing the dominant flow structures during this transitional regime TR (I)-(II).

We performed a transient analysis, plotting the SPOD time coefficients, their amplitude, the pressure signal and the averaged greyscale value, as well as space–time diagrams together. The data match very well, allowing us to link the SPOD modes to physical flow structures in the original flow field, as well as to get a deeper insight into the flow using the high-frequency pressure signal.

This image processing technique enables the extraction of spatial and temporal information through the analysis of greyscale values, presenting applicability to a range of fluid mechanics problems that require the analysis of high-speed recordings. SPOD enables the identification of the times at which modes occur by examining the time coefficients, allowing to analyse intermittent and multimodal behaviour. The accurate decomposition of the prevailing structures into physically relevant structures helps us to understand and interpret the underlying physics of the flow.

SPOD is capable of reconstructing the flow field using only a few modes, effectively capturing the main physics of the flow from high-speed images. Despite the data being greyscale values rather than physical quantities, SPOD provides valuable insights into the flow dynamics. In future work, SPOD can be applied to velocity fields from cloud cavitation, both experimentally and numerically generated, to decompose the flow and extract the kinetic energy associated with each mode. This will enable a statistical analysis of how frequently each mode occurs under specific flow conditions, offering deeper insights into the flow behaviour.

6 Supplementary information

Supplementary movies 1-8 are available. The data that support the findings of this study are available upon reasonable request from the authors. The SPOD software is available via the GitHub repository (https://github.com/grigorishat/SPyOD), Hatzissawidis and Sieber (2023).

Appendix A : Strouhal number *St* vs. cavitation numberσ

For each operation point in the shockwave-driven (I) and the re-entrant flow-driven (II) regime, as well as in the transition regime (I)-(II), the frequencies of the fundamental modes are calculated (Fig. 23). The classical approach provided by

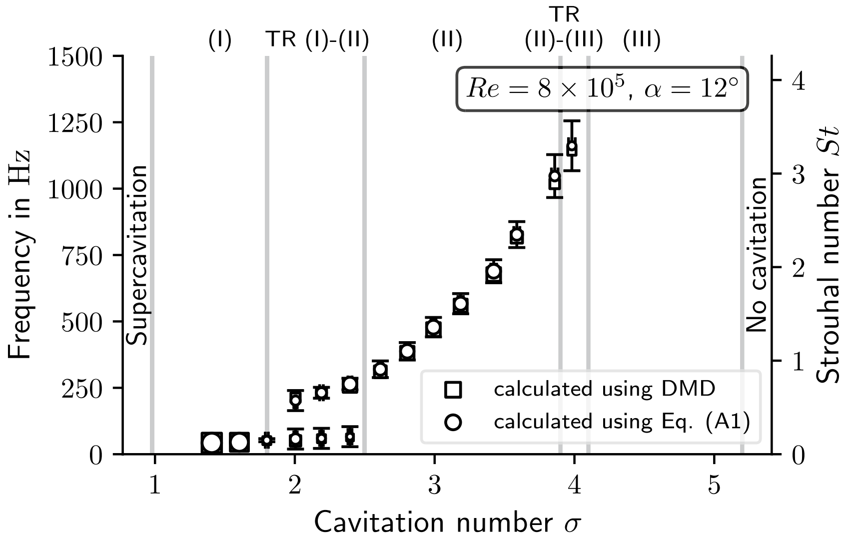

Fig. 23 Strouhal number and frequency of the modes associated with the low-frequency band and the high-frequency band, corresponding to shockwave-driven cloud cavitation (I) and re-entrant flow-driven cloud cavitation (II), at a constant Reynolds number $Re = 8 \times 10^5$ and incidence $\alpha = 12°$ for varying cavitation numbers σ. There are three dominant regimes, where the boundaries are denoted by the solid lines (—): (I) shockwave-driven cloud cavitation, (II) re-entrant flow-driven cloud cavitation and (III) sheet cavitation. Additionally, there are two transition regimes. The squares (□) are the frequencies of the fundamental mode calculated with the classic dynamic mode decomposition method, cf. Sieber et al. (2016). The circles (○) are the same frequencies calculated with Eqs. (15) and (A1), giving the weighted mean. The corresponding error bar is the weighted standard deviation Eq. (A2). The dot size represents the variance of the mode

Sieber et al. (2016) is to apply the dynamic mode decomposition (DMD) on the time coefficients. In this study, we adopted an alternative methodology to obtain the mean and standard deviation of the modal frequency. We calculate the gradient of the angle of the complex time coefficient, cf. Eq. (15), which corresponds to the frequency.

To obtain the mean value and the variance of the frequency f, we use the weighted arithmetic mean, using the amplitude of the complex time coefficient $\left|\tilde{b}(t_i)\right|$ at time t_i as weights, resulting in

$$\bar{f} = \frac{\sum_{i=1}^{N} \left|\tilde{b}(t_i)\right| f_i}{\sum_{i=1}^{N} \left|\tilde{b}(t_i)\right|}, \tag{A1}$$

and

$$\sigma^2(f) = \frac{\sum_{i=1}^{N} \left|\tilde{b}(t_i)\right| \left(f_i - \bar{f}\right)^2}{\sum_{i=1}^{N} \left|\tilde{b}(t_i)\right|}, \tag{A2}$$

respectively. For all SPOD calculations, the filter size is $2 - 3$ times the period of the fundamental mode.

Generally, the standard deviation of the frequency increases with increasing cavitation number σ (Fig. 23). The weighted standard deviation of the fundamental frequency $\sqrt{\sigma^2(f)}$ is between 2 % and 10 %, except for $\sigma = 2$, where it is 18 % of the mean of the fundamental frequency $\bar{f}$. This method allows to easily quantify a standard deviation for the frequency of each mode.

To illustrate the calculation, we plot the distribution of the Strouhal numbers as a histogram and calculate its kernel density estimation (KDE) for cavitation numbers from $\sigma = 1.4$ to $\sigma = 4.0$ (Fig. 24). The mean and standard deviation are weighted by the amplitude of the complex time coefficients $\left|\tilde{b}(t_i)\right|$ as before. The weighted mean of the Strouhal number $\overline{St}_1$ of the fundamental mode is calculated using Eq. (A1).

As SPOD permits frequency variations, which is a key benefit of the method, the Strouhal number constitutes a distribution. It is crucial to note that we obtain a unimodal distribution, indicating the successful decomposition of modes.

Appendix B: Pearson correlation coefficient

The Pearson correlation coefficient between two variables ζ and η is defined as

$$r_{\zeta,\eta} := \frac{\mathrm{Cov}(\zeta, \eta)}{\sigma(\zeta)\,\sigma(\eta)}, \tag{B3}$$

where $\mathrm{Cov}(\zeta, \eta)$ is the covariance between the two variables. Since the time coefficient $\tilde{b}$ is a complex value, the Pearson correlation coefficient is complex as well. The absolute value of Pearson correlation coefficient indicates the strength of

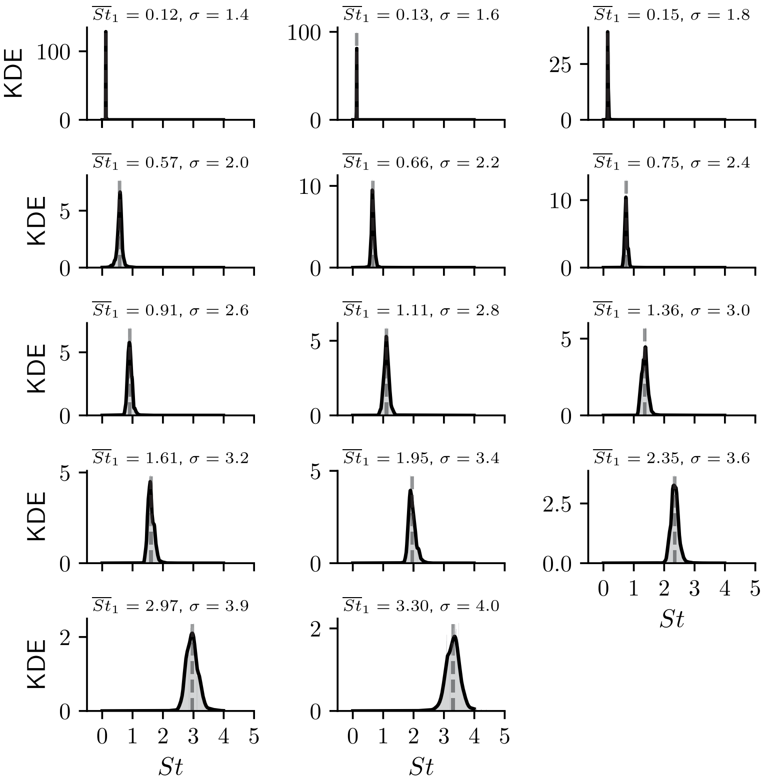

Fig. 24 Kernel density estimator (KDE) (——) of the Strouhal number *St* calculated with Eq. (15). The grey area is the weighted histogram of the frequencies calculated with Eq. (15). The weighted mean value (- - -) of the Strouhal number for the first mode $\overline{St}_1$ is given at the top of each subplot

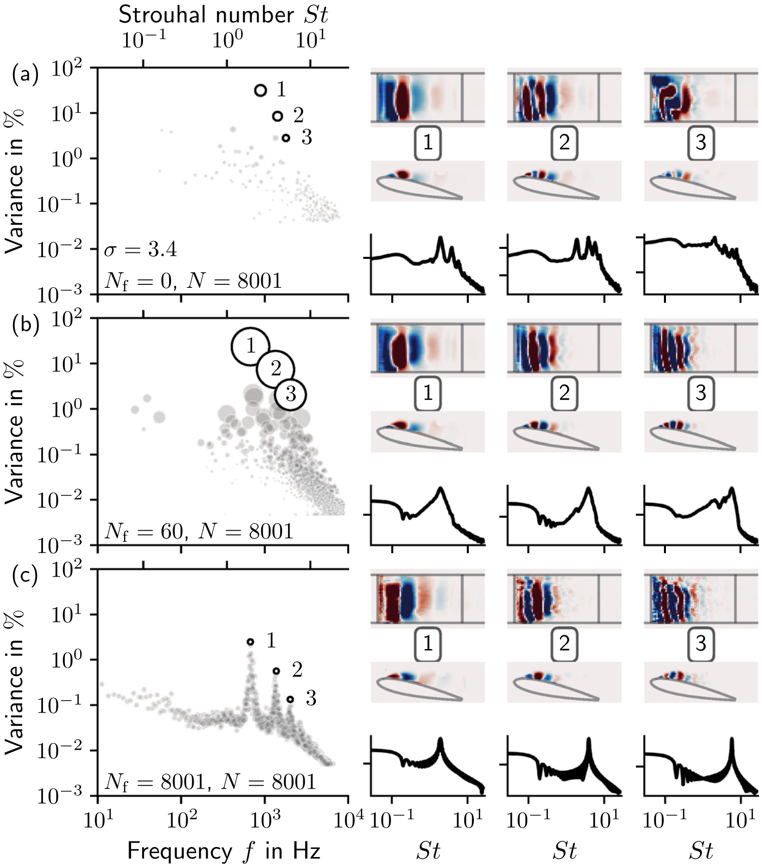

Fig. 25 SPOD spectrum, real part of the spatial modes and the Welch PSD of the real part of the temporal coefficients for $\sigma = 3.4$, regime (II): **a** POD: $N_\mathrm{f} = 0$, **b** SPOD: $N_\mathrm{f} = 60$ and **c** DFT: $N_\mathrm{f} = N = 8001$. A single dot in the SPOD spectrum corresponds to one mode pair, and the size is the harmonic correlation between them

the correlation and ranges from 0 (no correlation) to 1 (perfect correlation).

Appendix C : A comparison between POD, SPOD and DFT for regime (II)

A comparison between POD, SPOD and DFT for a cavitation number of $\sigma = 3.4$ shows the benefits of SPOD over the other two established methods. The spectra are plotted on the left-hand side for these three cases, respectively, denoted by **a**, **b** and **c** in Fig. 25. On the right-hand side, the real part of the mode from the top and side view and the Welch PSD of the real part of the time coefficient with a window size of 512 and an overlap of 50 % are plotted.

The POD analysis exhibits three dominant modes indicated by 1, 2 and 3 in the spectrum. The first mode is the main cloud shedding due to the re-entrant flow as expected, although there are higher harmonics in the PSD of the time coefficient. Mode 2 does not exhibit a clear peak in the PSD; rather, there are multiple peaks in the PSD. Mode 3 cannot be directly linked to a higher harmonic from its spatial mode, since it exhibits a mixture of different wavelengths, cf. Sieber et al. (2016).

The other extreme, which is the DFT, has the same full harmonic correlation between each mode pairs, since in the case of the DFT the analysis converges to sines and cosines for the temporal coefficients. Therefore, it is not possible to select the modes of interest based on the harmonic correlation. The three modes are depicted from the three visible peaks in the spectrum (Fig. 25c). Its variance is one order of magnitude lower than in the other two cases, indicating the swap of the mode in neighbouring modes when the frequency slightly changes.

In contrast to POD and DFT, SPOD shows a clear peak in each mode, forcing the POD in clear temporal dynamics, cf. Sieber et al. (2016). Mode 1 is the same as in the case of POD and DFT without the peaks at higher frequencies by decomposing this mode from the higher harmonics. Modes 2 and 3 show a clear peak contrary to POD. The spatial modes are clearer, not being corrupted by noise. It is now obvious that the second and third modes are the first and second harmonic of the first mode.

The successful decomposition, in contrast to POD and DFT, becomes more clear in the Lissajous curves for POD, SPOD and DFT (Fig. 26a–c, d–f, g–i), respectively. The first column (Fig. 26a, d, g) shows the real part against the imaginary part of the time coefficient of the first mode. The real and imaginary parts have a phase difference of about $\pi/2$, which results in a circle. Since in the case of DFT the time coefficients converge to sines and cosines, the result is a perfect circle (Fig. 26g), without any variation in the amplitude. In the case of POD (Fig. 26a), the circle is affected by noise. In the case of SPOD (Fig. 26d), the circle is approximated well, with small variations in amplitude, which are also detected in the high-speed recordings.

The second column (Fig. 26b, e, h) shows the Lissajous curve between mode 1 and mode 2. From the SPOD, it can be concluded that modes 1 and 2 have a phase difference between 0 and $\pi/4$. From the POD, the form looks asymmetric as in Fig. 26a. There is a phase drift in the case of DFT, which leads to a Lissajous curve that cannot be reasonably analysed (Fig. 26h).

The Lissajous curve of the first and third modes for the SPOD case shows that the third mode is triple the frequency with a phase difference between 0 and $\pi/4$ (Fig. 26f), as in Fig. 26e. Again, the Lissajous curve for the POD case is strongly corrupted, whereas the DFT shows a perfect curve.

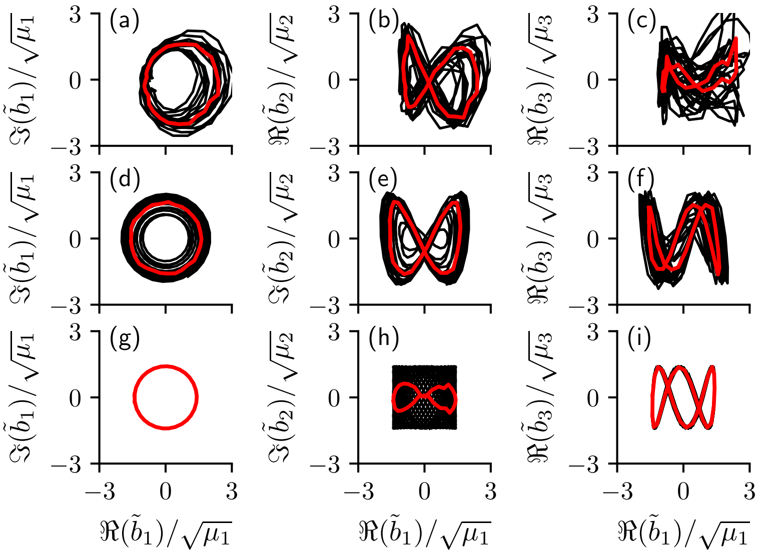

Fig. 26 Lissajous curves for **a**–**c** POD, **d**–**f** SPOD, **g**–**i** DFT between the real part of the first mode and its imaginary part, as well as the second and third mode. The time coefficients are scaled with the square root of their eigenvalues $\sqrt{\mu_i}$. The red line is the averaged curve over all cycles

From the SPOD spectra, the spatial modes, the PSD of the time coefficients, as well as the Lissajous curves, it can be concluded that SPOD is able to decompose the three modes from each other leading to spectra with a clear peak. Further, SPOD can eliminate the noise from the data. This approach permits variations in frequency and amplitude that are inherent in the original data.

For more details of the benefits of SPOD over POD and DFT, we refer to the examples in Sieber et al. (2016).

Appendix D : Inflow characterisation of the test section

Due to the test section's proximity to the pump and the small dimensions compared to other facilities, the inlet flow was characterised in detail using laser Doppler velocimetry (LDV) prior to conducting the main experiments presented in this paper. These preliminary studies were conducted using a one-dimensional LDV system. Specifically, the burst-spectrum analyser 57N10 and the probe 60X10, both manufactured by Dantec Dynamics, were employed. A solid-state laser—the Coherent Genesis MX 514 (STM-Series), operating at a wavelength of 514 nm—was utilised in the experiments. Hollow glass spheres with a mean particle diameter of 10 µm were used as tracer particles.

The experiments were conducted without a hydrofoil for an empty test section. The measurement plane, orthogonal to the bulk flow, was positioned at $x = 93$ mm upstream of the hydrofoil's axis of rotation. The Reynolds number was varied from 5.75×10^5 to 12.65×10^5 in increments of $\Delta Re = 5.75 \times 10^4$ resulting in 13 operation points. The static pressure was maintained at sufficiently high levels throughout the experiments to avoid cavitation.

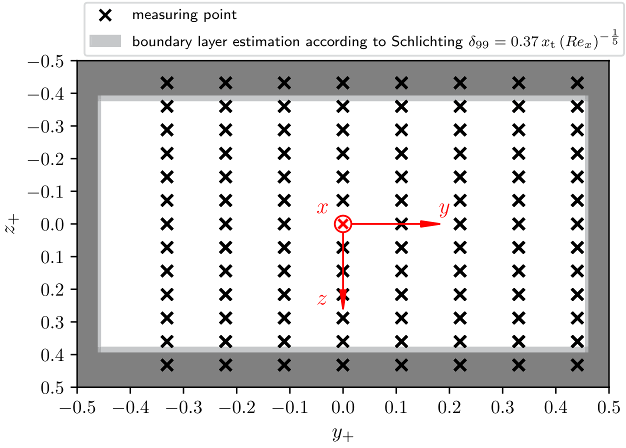

Fig. 27 Measurement plane at $x = 93$ mm upstream of the hydrofoil's axis of rotation. The bulk flow is in the positive x-direction. The laser is positioned at the right-hand side. The local velocity was measured at 13 location along the z-direction and 8 locations along the y-direction, resulting in a total of 104 measurements. The grey-filled area is the boundary layer thickness estimation according to Eq. (D4). The bright grey-filled area is the variation of the boundary layer thickness depending on the Reynolds number

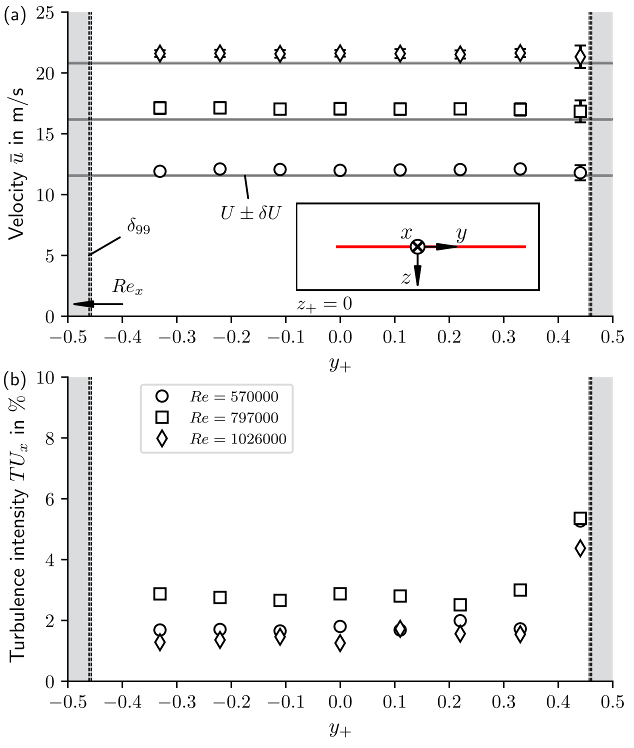

Fig. 28 The LDV results at $z_+ = 0$ are presented as follows: **a** The velocity profile, along with the mean velocity U derived from the volumetric flow rate, is shown, with the corresponding uncertainty indicated by horizontal lines. The boundary layer, calculated using Eq. (D4), exhibits a weak dependence on the considered Reynolds numbers Re_x, as shown by the arrow. **b** The turbulence intensity in the x-direction, computed using Eq. (D7), is also displayed. The velocities show good agreement, with an increase in the standard deviation of the velocity as the boundary layer is approached and a corresponding increase in turbulence intensity

The probe was positioned at 13 location along the z-direction and 8 locations along the y-direction using a cross-table from Isel with a repeat accuracy of 0.02 mm, resulting in a total of 104 measurements for each Reynolds number. The measurement plane with the measurement points is plotted in Fig. 27. The grey-filled area represents an estimation of the turbulent boundary layer thickness for a flat plate according to Schlichting (1965),

$$\delta_{99} = 0.37\,x_t \left(Re_x\right)^{-\frac{1}{5}} = 0.37\,x_t \left(\frac{U\,x_t}{\nu}\right)^{-\frac{1}{5}}, \tag{D4}$$

where x_t is the distance from the point where the boundary layer begins to form. This equation was also used by Holdhusen and Straub (1948) during the development of a

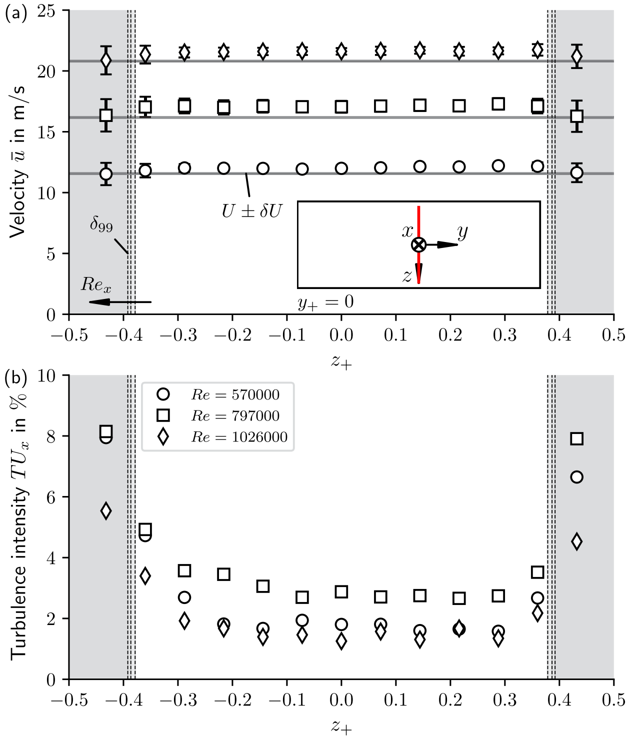

Fig. 29 The LDV results at $y_+ = 0$ are presented as follows: **a** The velocity profile, along with the mean velocity U derived from the volumetric flow rate, is shown, with the corresponding uncertainty indicated by horizontal lines. The boundary layer, calculated using Eq. (D4), exhibits a weak dependence on the considered Reynolds numbers Re_x, as shown by the arrow. **b** The turbulence intensity in the x-direction, computed using Eq. (D7), is also displayed. The velocities show good agreement, with a slight decrease in the velocity within the boundary layer and a corresponding increase in turbulence intensity

cavitation tunnel. The bright grey-filled area is the variation of the boundary layer thickness depending on the Reynolds number. The origin of the coordinate is located at the midpoint of the test section.

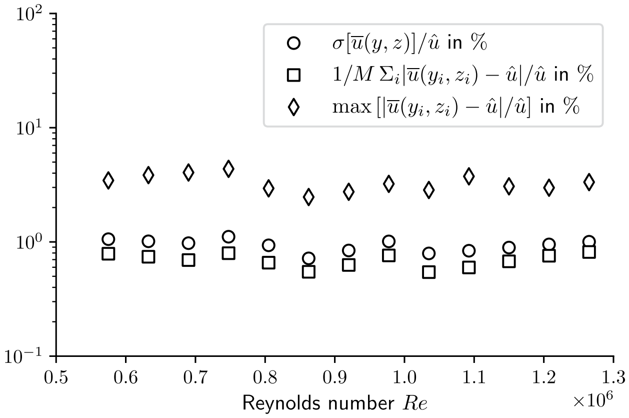

Fig. 30 Coefficient of variation (○), relative mean absolute difference (□) and relative maximum absolute difference (◊) of the LDV results over the Reynolds numbers investigated

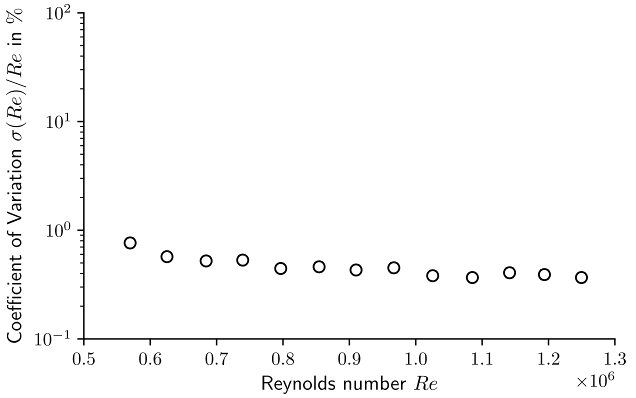

Fig. 31 Time-averaged Reynolds numbers against the corresponding coefficient of variation, as measured by the volumetric flow meter. The coefficient of variation remains lower than 1% across all operational points

First, we examine the spatial flow uniformity. For that purpose, we plot the velocity profile and the turbulence intensity in x-direction in the middle of the test section, $z_+ = 0$ and $y_+ = 0$ (Fig. 28 and Fig. 29a and b), respectively. The coordinates y and z are non-dimensionalised by the height H and the span b, i.e. $y_+ = y/H$ and $z_+ = z/b$, respectively. The positions of the plotted velocity profiles in the cross-sectional area are indicated by the red lines (Fig. 28a and Fig. 29a).

The boundary layer thickness according to Eq. (D4) decreases slightly with increasing Reynolds number, among the three values plotted, indicated by the arrow in Fig. 28a and Fig. 29a.

The velocity measured using LDV can be split into a time-averaged velocity and a fluctuation component, $u(y,z,t) = \overline{u}(y,z) + u'(y,z,t)$, with the time-averaged velocity calculated as

$$\overline{u}(y,z) = \frac{1}{N}\sum_{i=1}^{N} u(y,z,t_i), \tag{D5}$$

as shown in Fig. 28a and Fig. 29a with N being the number of time instances.

The error bars in Fig. 28a and Fig. 29a indicate the standard deviation of $u(y,z,t)$,

$$\sigma(u) = \sqrt{\overline{u'^2}} = \sqrt{\frac{1}{N}\sum_{i=1}^{N}\left[u(y,z,t_i) - \overline{u}(y,z)\right]^2}. \tag{D6}$$

Using these values, the turbulence intensity in x-direction (Figs. 28 and 29b) can be calculated as

$$TU_x = \frac{\sigma(u)}{\overline{u}}. \tag{D7}$$

It should be mentioned that bias errors arising from transit time effects—where faster-moving particles traverse the measurement volume more rapidly and pass through more frequently than their slower counterparts—are eliminated by weighting the velocity according to the transit time.

For comparison, the mean free-stream velocities U derived from the volumetric flow meter for the three Reynolds numbers along with their uncertainties δU as per the Guide to the Expression of Uncertainty in Measurements (GUM), ISO/TMBG Technical Management Board (2010), are plotted as horizontal lines alongside the velocities obtained from LDV (Figs. 28 and 29a).

The comparison between the velocities measured by the volumetric flow meter and the LDV shows good agreement (Figs. 28 and 29a). As the boundary layer is approached, the standard deviation of the velocity increases, accompanied by a corresponding increase in turbulence intensity, as shown in Fig. 28a and b. The measurements within the boundary layer show a slight decrease in velocity and an increase in turbulence intensity, as depicted in Fig. 29a and b. For a Reynolds number of $Re = 7.97 \times 10^5$, which is close to the value investigated in this study, the turbulence intensity in x-direction is approximately $3\,\%$ in the middle zone of the test section.

Next, we evaluate the uniformity across the entire measured plane. To do so, we define the combined time- and space-averaged velocity as

$$\hat{u} = \frac{1}{M}\sum_{i=1}^{M} \overline{u}(y_i, z_i) = \frac{1}{M}\sum_{j=1}^{M}\left[\frac{1}{N}\sum_{i=1}^{N} u(y_j, z_j, t_i)\right], \tag{D8}$$

where M is the number of spatial points. The coefficient of variation, defined as the ratio of the standard deviation of the time-averaged velocities in the plane to the combined mean, $\sigma[\overline{u}(y,z)]/\hat{u}$, is plotted over the investigated Reynolds numbers (Fig. 30) and remains consistently low at approximately 1%. In addition to the coefficient of variation, the relative mean absolute difference and the relative maximum absolute difference, defined as

$$\frac{1}{M}\sum_{i=1}^{M} \frac{|\overline{u}(y_i, z_i) - \hat{u}|}{\hat{u}}, \text{ and} \tag{D9}$$

$$\max\left[\frac{|\overline{u}(y_i, z_i) - \hat{u}|}{\hat{u}}\right], \tag{D10}$$

respectively, are also plotted in Fig. 30. These metrics further highlight the variability and extremes in the velocity field, with the former being around $1\,\%$ and the latter reaching 3%. Such low values confirm that the inflow conditions are uniform, validating the consistency of the flow.

For comparison, the Reynolds numbers derived from the volumetric flow meter against their corresponding coefficients of variation are shown in Fig. 31, consistently exhibiting values below 1% across all operational points investigated.

Supplementary Information The online version contains supplementary material available at https://doi.org/10.1007/s00348-024-03949-z.

Acknowledgements We kindly acknowledge the financial support by the Deutsche Forschungsgemeinschaft (DFG, German Research Foundation)-Project-ID 265191195-Collaborative Research Center 1194 (CRC 1194) "Interaction between Transport and Wetting Processes", project C06. The authors also gratefully acknowledge the support of the Federal Ministry for Economic Affairs and Climate Action (BMWK). The authors also thank Mr U. Trometer and Mr A. Schuler for the technical support and manufacturing of the specimens. We thank the anonymous reviewers for their helpful comments and suggestions to improve the quality of the paper.

Author Contributions Grigorios Hatzissawidis, Moritz Sieber and Peter F. Pelz were involved in conceptualisation; Grigorios Hatzissawidis and Moritz Sieber were responsible for methodology, software and writing—original draft; Grigorios Hatzissawidis performed investigation and visualisation; Peter F. Pelz acquired the funding; Grigorios Hatzissawidis, Moritz Sieber, Kilian Oberleithner and Peter F. Pelz took part in writing—reviewing and editing; and Kilian Oberleithner, Moritz Sieber and Peter F. Pelz participated in supervision.

Funding Open Access funding enabled and organized by Projekt DEAL. This work was supported by the Federal Ministry for Economic Affairs and Climate Action (BMWK) on the basis of a decision by the German Bundestag (Grant number: 20395 N).

Declarations

Conflict of interest The authors have no conflict of interest to declare that are relevant to the content of this article.

References

Arndt REA (2012) Some remarks on hydrofoil cavitation. J Hydrodyn 24(3):305–314. https://doi.org/10.1016/S1001-6058(11)60249-7

Arndt REA, Song CCS, Kjeldsen M, Keller A (2000) Instability of Partial Cavitation: A Numerical/Experimental Approach. In: Twenty-Third Symposium on Naval Hydrodynamics. National Academies Press, Val de Reuil, France, http://conservancy.umn.edu/handle/11299/49781

Barbaca L, Pearce BW, Ganesh H, Ceccio SL, Brandner PA (2019) On the unsteady behaviour of cavity flow over a two-dimensional wall-mounted fence. J Fluid Mech 874:483–525. https://doi.org/10.1017/JFM.2019.455

Barwey S, Ganesh H, Hassanaly M, Raman V, Ceccio S (2020) Data-based analysis of multimodal partial cavity shedding dynamics. Exp Fluids 61(4):98.https://doi.org/10.1007/S00348-020-2940-X

Bhatt A, Ganesh H, Ceccio SL (2023) Partial cavity shedding on a hydrofoil resulting from re-entrant flow and bubbly shock waves. J Fluid Mech 957:A28. https://doi.org/10.1017/JFM.2022.999

Bies DA, Hansen CH (2009) Engineering noise control: Theory and practice, fourth edition, CRC Press, London. https://doi.org/10.1201/9781315273464

Brennen CE (2013) Cavitation and bubble dynamics. Cambridge University Press, Cambridge. https://doi.org/10.1017/CBO9781107338760

Budich B, Schmidt SJ, Adams NA (2018) Numerical simulation and analysis of condensation shocks in cavitating flow. J Fluid Mech 838:759–813. https://doi.org/10.1017/JFM.2017.882

Callenaere M, Franc JP, Michel JM, Riondet M (2001) The cavitation instability induced by the development of a re-entrant jet. J Fluid Mech 444:223–256. https://doi.org/10.1017/S0022112001005420

Coutier-Delgosha O, Stutz B, Vabre A, Legoupil S (2007) Analysis of cavitating flow structure by experimental and numerical investigations. J Fluid Mech 578:171–222. https://doi.org/10.1017/S0022112007004934

Dular M, Petkovšek M (2015) On the mechanisms of cavitation erosion - Coupling high speed videos to damage patterns. Exp Therm Fluid Sci 68:359–370. https://doi.org/10.1016/J.EXPTHERMFLUSCI.2015.06.001

Franc JP, Michel JM (2005) Fundamentals of cavitation, fluid mechanics and its applications, vol 76. Springer, Netherlands. https://doi.org/10.1007/1-4020-2233-6

Furness RA, Hutton SP (1975) Experimental and theoretical studies of two-dimensional fixed-type cavities. J Fluids Eng 97(4):515–521. https://doi.org/10.1115/1.3448098

Ganesh H, Mäkiharju SA, Ceccio SL (2016) Bubbly shock propagation as a mechanism for sheet-to-cloud transition of partial cavities. J Fluid Mech 802:37–78. https://doi.org/10.1017/JFM.2016.425

Gopalan S, Katz J (2000) Flow structure and modeling issues in the closure region of attached cavitation. Phys Fluids 12(4):895–911. https://doi.org/10.1063/1.870344

Hatzissawidis G, Sieber M (2023) grigorishat/SPyOD: 0.1.7. https://doi.org/10.5281/ZENODO.8077469

Hatzissawidis G, Ludwig GJ, Pelz PF (2021) Modal decomposition of large- and small-scale cloud cavitation. In: IOP Conference Series: Earth and Environmental Science, 774:12097, https://doi.org/10.1088/1755-1315/774/1/012097

Hatzissawidis G, Kerres L, Ludwig GJ, Pelz PF (2022) Spatiotemporal analysis of sheet and cloud cavitation and its damage potential. In IOP Conference Series: Earth and Environmental Science 1079(1):012046. https://doi.org/10.1088/1755-1315/1079/1/012046

Hatzissawidis G, Kuhr MMG, Pelz PF (2025) The transition from re-entrant flow-driven to shockwave-driven cloud cavitation. J Fluid Mech 1004:A13 https://doi.org/10.1017/jfm.2024.1224

Holdhusen JS, Straub LG (1948) Model Experiments for the Design of a Sixty Inch Water Tunnel Part III Test Section and Cavitation Index Studies. Tech. rep., St. Anthony Falls Hydraulic Laboratory, University of Minnesota, http://conservancy.umn.edu/handle/11299/108112

Holmes P, Lumley JL, Berkooz G, Rowley C (2012) Turbulence, coherent structures, dynamical systems and symmetry, 2nd edn. Cambridge University Press, Cambridge. https://doi.org/10.1017/CBO9780511919701

ISO/TMBG Technical Management Board (2010) ISO/IEC Guide 98–3:2008

ITTC (2016) ITTC - Recommended Procedures and Guidelines: Propulsion; Cavitation: Cavitation Induced Erosion on Propellers, Rudders and Appendages Model Scale Experiments (7.5-02 03-03.5). Tech. rep., International Towing Tank Conference (ITTC), http://ittc.info/media/1613/75-02-03-035.pdf

Jakobsen JK (1964) On the mechanism of head breakdown in cavitating inducers. J Basic Eng 86(2):291–305. https://doi.org/10.1115/1.3653066

Katsuno ET, Dantas JLD (2022) Blockage effect influence on model-scale marine propeller performance and cavitation pattern. Appl Ocean Res 120:103019. https://doi.org/10.1016/J.APOR.2021.103019

Kawanami Y, Kato H, Yamaguchi H, Tanimura M, Tagaya Y (1997) Mechanism and control of cloud cavitation. J Fluids Eng 119(4):788–794. https://doi.org/10.1115/1.2819499

Keil T (2014) Theoretische und experimentelle Untersuchungen der Schicht- und Wolkenkavitation. PhD thesis, Technische Universität Darmstadt, Darmstadt, https://doi.org/10.26083/TUPRINTS-00021344

Kjeldsen M, Arndt RE, Effertz M (2000) Spectral characteristics of sheet/cloud cavitation. J Fluids Eng 122(3):481–487. https://doi.org/10.1115/1.1287854

Knapp RT (1955) Recent investigations of the mechanics of cavitation and cavitation damage. J Fluids Eng 77(7):1045–1054. https://doi.org/10.1115/1.4014586

Knapp RT (1956) Further Studies of the Mechanics and Potential of Fixed Type Cavities. In: Symposium on cavitation in Hydrodynamics. Her Majesty's Stationary Office, London, https://resolver.caltech.edu/CaltechAUTHORS:20140820-111351580

Laberteaux KR, Ceccio SL (2001) Partial cavity flows. Part 1. Cavities forming on models without spanwise variation. J Fluid Mech 431:1–41. https://doi.org/10.1017/S0022112000002925

Leroux JB, Coutier-Delgosha O, Astolfi JA (2005) A joint experimental and numerical study of mechanisms associated to instability of partial cavitation on two-dimensional hydrofoil. Phys Fluids 17(5):052101. https://doi.org/10.1063/1.1865692

Lumley JL (1970) Stochastic tools in turbulence. Academic Press, New York

Pelz PF, Keil T, Groß TF (2017) The transition from sheet to cloud cavitation. J Fluid Mech 817:439–454. https://doi.org/10.1017/JFM.2017.75

Petkovšek M, Dular M (2013) Simultaneous observation of cavitation structures and cavitation erosion. Wear 300(1–2):55–64. https://doi.org/10.1016/J.WEAR.2013.01.106

Pham TM, Larrarte F, Fruman DH (1999) Investigation of unsteady sheet cavitation and cloud cavitation mechanisms. J Fluids Eng 121(2):289–296. https://doi.org/10.1115/1.2822206

Prothin S, Billard JY, Djeridi H (2016) Image processing using proper orthogonal and dynamic mode decompositions for the study of cavitation developing on a NACA0015 foil. Exp Fluids 57(10):157. https://doi.org/10.1007/S00348-016-2246-1

Reisman GE, Wang YC, Brennen CE (1998) Observations of shock waves in cloud cavitation. J Fluid Mech 355:255–283. https://doi.org/10.1017/S0022112097007830

Ronneberger O, Fischer P, Brox T (2015) U-net: Convolutional networks for biomedical image segmentation. Lecture Notes in Computer Science (including subseries Lecture Notes in Artificial Intelligence and Lecture Notes in Bioinformatics) 9351:234–241. https://doi.org/10.1007/978-3-319-24574-4_28

Schlichting H (1965) Grenzschicht-Theorie, 5th edn. G Braun, Karlsruhe

Schmid PJ (2010) Dynamic mode decomposition of numerical and experimental data. J Fluid Mech 656:5–28. https://doi.org/10.1017/S0022112010001217

Sieber M, Paschereit CO, Oberleithner K (2016) Spectral proper orthogonal decomposition. J Fluid Mech 792:798–828. https://doi.org/10.1017/JFM.2016.103

Sieber M, Paschereit CO, Oberleithner K (2021) Stochastic modelling of a noise-driven global instability in a turbulent swirling jet. J Fluid Mech 916:A7. https://doi.org/10.1017/JFM.2021.133

Sirovich L (1987) Turbulence and the dynamics of coherent structures. I. Coherent structures. Q Appl Math 45(3):561–571. https://doi.org/10.1090/QAM/910462

Smith SM, Venning JA, Pearce BW, Young YL, Brandner PA (2020) The influence of fluid-structure interaction on cloud cavitation about a flexible hydrofoil Part 2. J Fluid Mech 897:A28. https://doi.org/10.1017/JFM.2020.323

Smith SM, Venning JA, Pearce BW, Young YL, Brandner PA (2020) The influence of fluid-structure interaction on cloud cavitation about a stiff hydrofoil. Part 1. J Fluid Mech 896:A1. https://doi.org/10.1017/JFM.2020.321

Stutz B, Reboud JL (1997) Experiments on unsteady cavitation. Exp Fluids 22(3):191–198. https://doi.org/10.1007/s003480050037

Taira K, Brunton SL, Dawson ST, Rowley CW, Colonius T, McKeon BJ, Schmidt OT, Gordeyev S, Theofilis V, Ukeiley LS (2017) Modal analysis of fluid flows: an overview. AIAA J 55(12):4013–4041. https://doi.org/10.2514/1.J056060

Towne A, Schmidt OT, Colonius T (2018) Spectral proper orthogonal decomposition and its relationship to dynamic mode decomposition and resolvent analysis. J Fluid Mech 847:821–867. https://doi.org/10.1017/JFM.2018.283

Tu JH, Rowley CW, Luchtenburg DM, Brunton SL, Kutz JN (2014) On dynamic mode decomposition: theory and applications. J Comput Dyn 1(2):391–421. https://doi.org/10.3934/JCD.2014.1.391

Vaca-Revelo D, Gnanaskandan A (2023) Numerical assessment of the condensation shock mechanism in sheet to cloud cavitation transition. Int J Multiph Flow 169:104616. https://doi.org/10.1016/J.IJMULTIPHASEFLOW.2023.104616

Venning JA, Pearce BW, Brandner PA (2022) Nucleation effects on cloud cavitation about a hydrofoil. J Fluid Mech 947:A1. https://doi.org/10.1017/JFM.2022.535

Wade RB, Acosta AJ (1966) Experimental observations on the flow past a plano-convex hydrofoil. J Basic Eng 88(1):273–282. https://doi.org/10.1115/1.3645828

Wu J, Ganesh H, Ceccio S (2019) Multimodal partial cavity shedding on a two-dimensional hydrofoil and its relation to the presence of bubbly shocks. Exp Fluids 60(4):66. https://doi.org/10.1007/S00348-019-2706-5

Zhang G, Zhang D, Ge M, Petkovšek M, Coutier-Delgosha O (2022) Experimental investigation of three distinct mechanisms for the transition from sheet to cloud cavitation. Int J Heat Mass Transf 197:123372. https://doi.org/10.1016/J.IJHEATMASSTRANSFER.2022.123372